THE DISCRETE DIPOLE APPROXIMATION WITH SURFACE INTERACTION FOR EVANESCENT WAVE-BASED CHARACTERIZATION OF NANOSTRUCTURES ON A SURFACE WITH VALIDATION AGAINST EXPERIMENTAL RESULTS

by

Mitchell R. Short

A thesis submitted to the faculty of
The University of Utah
in partial fulfillment of the requirements for the degree of

Master of Science

Department of Mechanical Engineering

The University of Utah

August 2013

The University of Utah Graduate School

STATEMENT OF THESIS APPROVAL

The thesis of **Mitchell R. Short**

has been approved by the following supervisory committee members:

Mathieu Francoeur	, Chair	**May 2, 2013** Date Approved
Kent Udell	, Member	Date Approved
Ian Harvey	, Member	**May 2, 2013** Date Approved

and by **Tim Ameel**, Chair of the Department of **Mechanical Engineering**

and by Donna M. White, Interim Dean of The Graduate School.

ABSTRACT

Nanotechnology has become so widely used it can be found in every aspect of life, from cell-phones and computers, to cars, and even athletic socks. As it permeates so many markets, the need for supplemental technologies has also increased. One such needed technology is in the area of nanoscale characterization. Current imaging methods are advanced; however, they do not have the capabilities to characterize the size, shape, composition, and arrangement of nanostructures and nanoparticles in a real-time, unobtrusive manner. The Polarized-Surface-Wave-Scattering system (PSWSS) is a method being researched at the University of Utah that can provide such characterization, although in order for the PSWSS to function accurately through inversion techniques, a predictive forward model must be developed and validated. This work explores the discrete dipole approximation with surface interaction (DDA-SI), an open source *MATLAB* toolbox, as a predictive model to calculate electromagnetic scattering by objects on a surface illuminated by an evanescent wave generated by total internal reflection (TIR). Far-field scattering predictions via DDA-SI are validated against scaled microwave experimental results for two objects on a surface: a sphere with a diameter of $\lambda/1.92$ and a cube with a side length of $\lambda/1.785$, where λ refers to the wavelength. A good agreement between experiments and simulations is observed, especially when modified Fresnel reflection coefficients are employed by DDA-SI. Programs to calculate the amplitude scattering matrix and Mueller matrix elements have been also been created.

Additionally, the sensitivity of four Mueller matrix elements (M_{11}, M_{12}, M_{21}, and M_{22}) to the particle size, material (gold and silver), shape (sphere and cube), and interparticle spacing, is analyzed. It is found that these four elements are sensitive to changes in shape and interparticle spacing, whereas prove insufficient to difference in material and sizes smaller than one-half the wavelength of incident light. Findings show that DDA-SI is a strong forward model for calculation of far-field scattering, but for characterization purposes, other Mueller matrix elements that measure changes in circular polarization must be analyzed. Future research efforts will include more extensive experimental measurements and calibration, as well as creation of a scattering profile database, and further sensitivity analysis using DDA-SI.

TABLE OF CONTENTS

LIST OF FIGURES

NOMENCLATURE

Acronyms

AFM	Atomic force microscope
DDA	Discrete dipole approximation
DDA-SI	Discrete dipole approximation with surface interaction
JQSRT	*Journal of Quantitative Spectroscopy and Radiative Transfer*
LDR	Lattice dispersion relation
LP	Linear polarizer
MEMS	Micro-electro-mechanical systems
NIA	Normal incidence approximation
PA6	Polyamide
PE	Polyethylene
PSWSS	Polarized-surface-wave-scattering system
QWP	Quarter wave plate
SEM	Scanning electron microscope
STM	Scanning tunneling microscope
TE	Transverse electric
TIR	Total internal reflection
TM	Transverse magnetic

Symbols

$\underline{\underline{\alpha_j}}$	Polarizability
$\underline{\underline{\mathbf{A}}}$	Interaction matrix
ε_0	Permittivity of a vacuum
$\mathbf{e}_1$	Unit vector, TM polarization
$\mathbf{e}_2$	Unit vector, TE polarization
E_0	Fixed amplitude of the electric field
$\overline{\mathbf{E}}_{inc}$	Incident electric field vector
$\mathbf{E}_{sca}^{TE}$	Scattered field in TE polarization
$\mathbf{E}_x$	Electric field in the x-direction
$\mathbf{E}_y$	Electric field in the y-direction
γ_{crit}	Critical angle as determined by Snell's Law
γ_{inc}	Angle of incidence measured from normal
γ_r	Reflected angle
I,Q,U,V	Stokes parameters
I_{sca}	Intensity, scattered field
I_{inc}	Intensity, incident field

k	Wavevector
k_0	Wavevector magnitude in air
$\mathbf{k}_{sca}$	Scattered wavevector
$\mathbf{k}_{I,sca}$	Scattered wavevector image
λ	Wavelength
M_{ij}	Normalized Mueller matrix elements (i,j=1 to 4)
$\overline{\overline{\mathbf{M}}}$	Mueller Matrix
n_i	Refractive index of object
n_1	Refractive index of substrate
n_2	Refractive index of air
n_{Au}	Refractive index of gold
n_{Ag}	Refractive index of silver
N	Number of point dipoles
ω	Angular frequency
$\mathbf{p}_j$	Dipole moment at dipole j
$\mathbf{p}_j^{(1)}$	Dipole moment from TM incident field
$\mathbf{p}_j^{(2)}$	Dipole moment from TE incident field
$\overline{\mathbf{P}}$	Dipole moment vector
ϕ	Azimuthal angle
r^{TM}	Fresnel reflection coefficient, TM polarization
r^{TE}	Fresnel reflection coefficient, TE polarization
$\mathbf{r}_j$	Coordinates of dipole j
$\mathbf{r}_{I,j}$	Coordinates of image dipole j
$\overline{\overline{\mathbf{R}}}$	Surface interaction matrix
$\mathbf{S}$	Stokes vector
$\overline{\overline{\mathbf{S}}}$	Amplitude scattering matrix
S_j	Amplitude scattering matrix elements (j = 1 to 4)
θ_{scat}	Angle of scattered field, polar

CHAPTER 1

INTRODUCTION

The use of nanoscale materials and nanotechnology continues to grow rapidly all around the globe. Uses range from semiconductor fabrication for electronics, micro-electro-mechanical systems (MEMS) in projector mirrors or accelerometers in phones and cars, and anti-odor nanoparticles in socks or plastic food containers [1]. The technology of the world is shrinking down to the nanoscale, and in doing so, the ability to image, characterize, and validate these materials is critical. Imaging a material at this scale can be done in a variety of ways, including a scanning electron microscope (SEM) [1], an atomic force microscope (AFM) [2], or a scanning tunneling microscope (STM) [3]. These methods are well established and can provide excellent images at a very small scale, but they have certain limitations. SEM, for example, requires a conductive surface to function. This means that the material must already be conductive or must be coated with a conductive material. AFM, on the other hand, does not require a conductive material, but is limited to a topographical image and can damage the sample if run in a contact mode of operation. STM can even provide atomic scale resolution, but needs both a conducting surface and is limited to a topographical view [1]. The fact is, none of these methods provide characterization of nanostructures in a real-time and unobtrusive manner.

One characterization method being researched at the University of Utah to supplement current imaging technologies is the Polarized-Surface-Wave-Scattering System (PSWSS) [4-11]. This system is not meant to provide a visual output image such as the systems mentioned, but to supplement these imaging methods by providing a concise rundown of desired characteristics such as the size, shape, and arrangement of nanoparticles or structures on a surface. The PSWSS framework, depicted in Fig. 1.1, consists of nanostructures on a surface illuminated by an incident evanescent wave, or a surface wave, generated by total internal reflection (TIR) of a laser beam [11,12]. This evanescent wave decays exponentially over a distance of about one wavelength away from the surface, which creates an upper limit to the size of objects that can be characterized. However, it also enables subwavelength characterization of objects and overcomes the diffraction limit of many optical systems [12]. For simplicity, cubes and spheres are shown in Fig. 1.1; however, the PSWSS is intended to be used to characterize many complex-shape nanostructures. Additionally, the PSWSS is unobtrusive by measuring the far-field scattering profiles of the scattered evanescent wave, and is expected to be sensitive to the size, shape, composition, and arrangement of the nanostructures through use of the Mueller matrix elements. When the wave is scattered, it undergoes a change in polarization and directional intensity that is unique to the scatterer. The Mueller matrix is a 4 by 4 matrix that represents this change in polarization and directional intensity. By measuring the intensity of the incident and scattered fields through various combinations of linear polarizers (LP) and quarter wave plates (QWP), these 16 elements are experimentally measurable [13]. Similarly, they can be calculated by knowing the intensity and polarization state of the incident and scattered fields

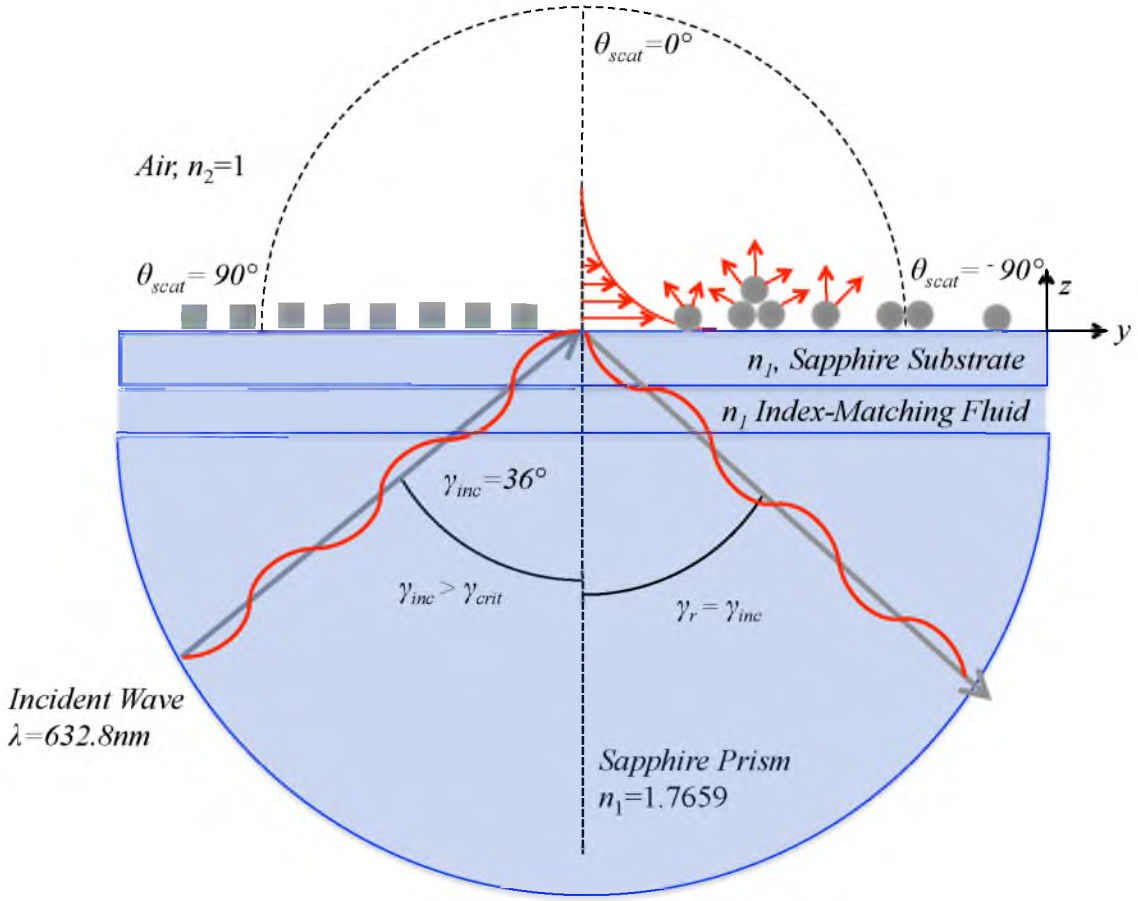

Figure 1.1: Schematic of the PSWSS with nanostructures on a surface illuminated by an evanescent wave generated by TIR.

[11,13]. All 16 elements may not be needed for characterization purposes; however, further analysis is necessary and is discussed throughout this work. A more in-depth look at the fundamentals of polarization, the Stokes parameters, and the Mueller matrix elements is provided in Appendix A. Furthermore, the time needed to run the PSWSS is primarily limited by the speed of the detector. As such, the system can make measurements in near real-time, whereas the imaging methods mentioned above have a significant limitation by lengthy measurement times. Nanoparticles have a tendency to agglomerate with one-another, and often quickly. Detecting this agglomeration is difficult

or impossible for current imaging technologies given the time needed for measurements, whereas the PSWSS will be able to make these measurements.

There are many possible applications of the PSWSS; however, there are specific areas the system can quickly have an impact. In a manufacturing environment, the characteristics of a sample are not completely unknown, but the quality of certain traits needs to be tightly controlled. Consider a case where gold nanoparticles are to be fabricated within a certain size range. In this situation, the material composition of the particle is known, but there needs to be an assurance the particles are within the acceptable sizes. The same situation could arise in many industries, such as measuring and controlling the height of carbon nanotubes on a surface. The PSWSS could have an impact in two different aspects of these situations. In the development stage, the PSWSS could be used to measure the samples while they are being fabricated, such that multiple trial runs would not be necessary to get the proper reaction time or fabrication time. Then once the samples are being produced to the required parameters, the PSWSS could be used as a quality-control measure. Because of the speed of measurements, and unobtrusive nature of the system, the PSWSS could be used to verify that all structures are within acceptable size, shape, or arrangement. The potential of the PSWSS is very promising, but because the framework relies upon inversion techniques [8-10] characterization from the PSWSS is only as accurate as the forward model used for the inversion.

Inversion techniques employed by the PSWSS have three essential parts, as depicted in Fig. 1.2: the forward model, the scattering profile database, and the inversion algorithm. These are all essential for characterization [11]. Computational modeling of

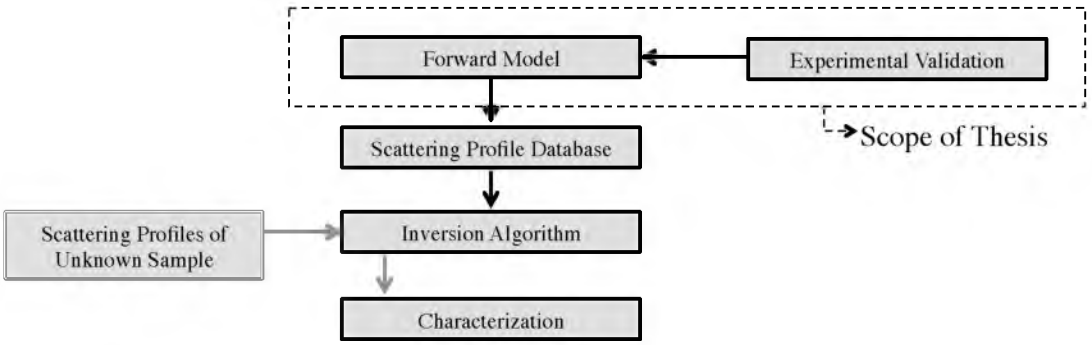

Figure 1.2: Diagram of inversion procedure for characterization using the PSWSS.

the scattering is used as a forward model to build the scattering profile database, a database that correlates varying characteristics to their corresponding scattering profiles [8-10]. By measuring the scattering profile of known samples, experimental results are used to validate this forward model. Then, using the database assembled from the forward model, an inversion algorithm will be employed to back-calculate characteristics from scattering profiles measured by the PSWSS from an unknown source (path shown in grey lines). This shows how the forward model is the foundation of the entire characterization methodology. If the forward model yields inaccurate results, then the database will not be accurate, and if the algorithm pulls from an inaccurate database, characterization will not be correct.

Prediction of evanescent wave scattering by particles on a surface is a challenging problem. This is in contrast to calculation of scattering by particles in suspension from direct illumination. Direct illumination of particles in suspension is less complex due more extensive research and approaches such as Mie theory, a widely known and accepted theory for calculating scattering by a spherical particle which can be extended using various methods to multiple particles [13,14]. Due to the presence of the surface,

additional interactions must be accounted for both in the incident field and the scattered far field. There is also added complexity from evanescent illumination. Previously, the T-matrix method combined with the normal incidence approximation (NIA) has been used to predict scattering by a sphere on a surface illuminated by a propagating [15,16] and an evanescent [4-7] wave. An exact solution for the problem of multiple spheres on a surface was also proposed by Mackowski [17]. For characterization purposes, the forward model should be able to accommodate arbitrarily shaped objects on a surface. Numerical approaches such as the null-field method with discrete sources [18] and the finite-difference time-domain method [19] could be employed for that purpose. In this work, evanescent wave scattering by nanostructures on a surface is predicted via the discrete dipole approximation (DDA). DDA is a widely accepted method of solving light scattering by particles from direct propagating illumination. The most well-known application is by Draine and Flatau in the open-source code DDSCAT written in *Fortran* [20,21]. Similarly, ADDA is an open-source *C* software package developed by Yurkin and Hoekstra [22,23]. These codes, however, do not accommodate for evanescent illumination of particles on a surface.

The method being evaluated for the forward model to be used in the PSWSS is the discrete dipole approximation with surface interaction (DDA-SI) developed by Loke et al. [24,25]. DDA-SI was created as an open-source *MATLAB* computational toolbox [26] and is based on the work of Schmehl [27]. DDA-SI has been chosen both for its accuracy as well as its flexibility. DDA-SI is based on discretizing the objects into point electric dipoles, and because calculations are made for each individual dipole, it can accommodate any complex-shape scatterer. This can vary from simple geometries such

as cylinders, cubes, and spheres, to more complex agglomerates or arrays of particles. Additionally, DDA-SI can be used both for cases of propagating and evanescent illuminations.

The objective of this thesis is to use, expand, and experimentally validate the DDA-SI program package for calculations of far-field scattering and Mueller matrix elements by objects on a surface illuminated by an evanescent wave. This is done with the goal of using DDA-SI as the forward model for characterization via the PSWSS. To do this, results provided by DDA-SI are validated against scattering profiles measured at microwave frequencies at the Institut Fresnel in Marseille, France. Because of the formalism of DDA-SI, and the linearity of Maxwell's equations, the problem can be scaled relative to the wavelength for any part of the electromagnetic spectrum. This was performed because characteristics in the microwave regime are far more easily measured and controlled due to the scale (centimeters rather than nanometers or micrometers), as can be seen in Figure. 1.3.

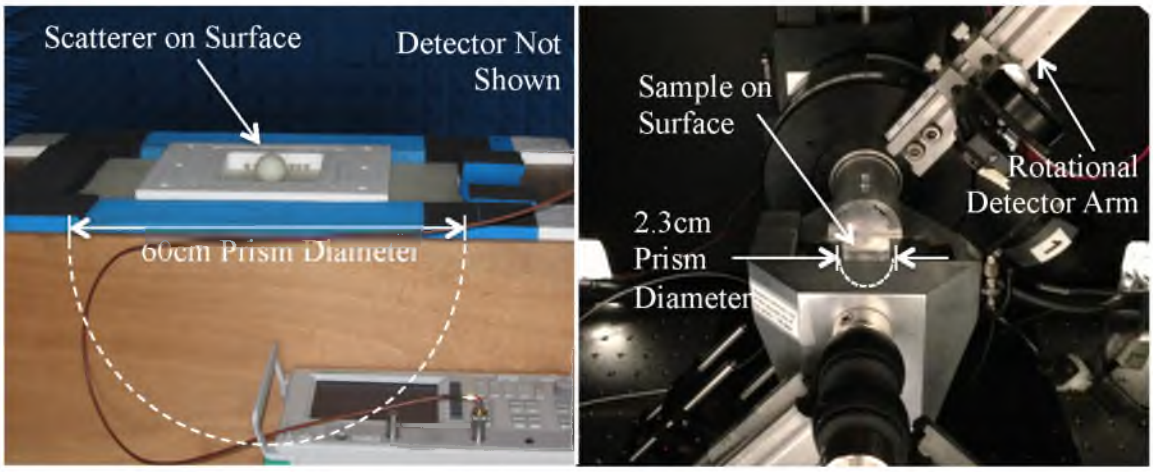

Figure 1.3: Comparison of microwave analogy (left) with the PSWSS optical set-up (right).

Comparison with experimental results also uncovered areas of DDA-SI that needed to be expanded and improved upon, and are outlined below. Subsequently, the sensitivity of four Mueller matrix elements (M_{11}, M_{12}, M_{21}, M_{22}) is analyzed for gold and silver nanoparticles via DDA-SI for application to the PSWSS and setting up calibration samples. This work is presented in the next chapter as a stand-alone paper submitted to be published in the *Journal of Quantitative Spectroscopy and Radiative Transfer*. Through this work, the PSWSS is one step closer to being a powerful nanoscale characterization tool to supplement current imaging technologies using DDA-SI as a forward model. A summary of findings, recommendations, and future plans are found in Chapter 3. Also included are the fundamentals of wave polarization, the Stokes parameters, and Mueller matrix elements in Appendix A, and the added and modified *MATLAB* programs in Appendices B to F.

1.1 References

[1] Madou M.J., *Fundamentals of Microfabrication and Nanotechnology*, CRC Press, Florida, 2012.

[2] Binnig G. and Quate C.F., Atomic force microscopy, *Physical Review Letters* **56**, 930-933, 1986.

[3] Binnig G., Rohrer H., Gerber Ch., and Weibel E., Surface studies by scanning tunneling microscopy, *Physical Review Letters* **49**, 57-61, 1982.

[4] Videen G., Aslan M.M. and Mengüç M.P., Characterization of metallic nano-particles via surface wave scattering: A. Theoretical framework and formulation, *Journal of Quantitative Spectroscopy and Radiative Transfer* **93**, 195-206, 2005.

[5] Aslan M.M., Mengüç M.P. and Videen G., Characterization of metallic nano-particles via surface wave scattering: B. Physical concept and numerical experiments, *Journal of Quantitative Spectroscopy and Radiative Transfer* **93**, 207-217, 2005.

[6] Venkata P.G., Aslan M.M., Mengüç M.P. and Videen G., Surface plasmon scattering patterns of gold nanoparticles and 2D agglomerates, *ASME Journal of Heat Transfer* **129**, 60-70, 2007.

[7] Francoeur M., Venkata P.G. and Mengüç M.P., Sensitivity analysis for characterization of gold nanoparticles and agglomerates via surface Plasmon scattering patterns, *Journal of Quantitative Spectroscopy and Radiative Transfer* **106**, 44-55, 2007.

[8] Charnigo R., Francoeur M., Mengüç M.P., Brock A., Leichter M. and Srinivasan C., Derivatives of scattering profiles: Tools for nanoparticle characterization, *Journal of the Optical Society of America A* **24**, 2578-2589, 2007.

[9] Charnigo R., Francoeur M., Kenkel P., Mengüç M.P., Hall B. and Srinivasan C., Estimating quantitative features of nanoparticles using multiple derivatives of scattering profiles, *Journal of Quantitative Spectroscopy and Radiative Transfer* **112**, 1369-1382, 2011.

[10] Charnigo R., Francoeur M., Kenkel P., Mengüç M.P., Hall B. and Srinivasan C., Credible intervals for nanoparticle characteristics, *Journal of Quantitative Spectroscopy and Radiative Transfer* **113**, 182-193, 2011.

[11] Francoeur M., Near-Field Radiative Transfer: Thermal Radiation, Thermophotovoltaic Power Generation and Optical Characterization, PhD Dissertation, University of Kentucky, 2010.

[12] Hecht E., *Optics*, Pearson Education Inc., California, 2002.

[13] Bohren C.F. and Huffman D.R., *Absorption and Scattering of Light by Small Particles*, Wiley, New York, 1983.

[14] Mischenko M.I., Travis L.D., and Lacis A.A., *Multiple Scattering of Light by Particles: Radiative Transfer and Coherent Backscattering*, Cambridge University Press, New York, 2006.

[15] Videen G., Light scattering from a sphere on or near a surface, *Journal of the Optical Society of America A* **8**, 483-499, 1991.

[16] Videen G., Turner M.G., Iafelice V.J., Bickel W.S. and Wolfe W.L., Scattering from a sphere near a surface, *Journal of the Optical Society of America A* **10**, 118-126, 1993.

[17] Mackowski D.W., Exact solution for the scattering and absorption properties of sphere clusters on a plane surface, *Journal of Quantitative Spectroscopy and Radiative Transfer* **109**, 770-788, 2008.

[18] A. Doicu, T. Wriedt and Y.A. Eremin, *Light Scattering by Systems of Particles*, Springer, 2006.

[19] Muller J., Parent G., Jeandel G. and Lacroix D., Finite-difference time-domain and near-field-to-far-field transformation in the spectral domain: Application to scattering objects with complex shapes in the vicinity of a semi-infinite dielectric medium, *Journal of the Optical Society of America A* **28**, 868-878, 2011.

[20] Flatau P.J. and Draine B.T., Discrete dipole approximation for scattering calculations, *Journal of the Optical Society of America A* **11**, 1491-1499, 1994.

[21] Draine, B.T. and Flatau, P.J., User guide to the discrete dipole approximation code DDSCAT 7.2, http://arXiv.org/abs/1202.3424, 2012.

[22] Hoekstra A.G. and Yurkin M.A., The discrete-dipole-approximation code ADDA: Capabilities and known limitations, *Journal of Quantitative Spectroscopy and Radiative Transfer* **112**, 2234-2247, 2011.

[23] Yurkin M.A. and Hoekstra A.G., The discrete dipole approximation: An overview and recent developments, *Journal of Quantitative Spectroscopy and Radiative Transfer* **106**, 558-589, 2007.

[24] Loke V.L.Y. and Mengüç M.P., Surface waves and atomic force microscope probe-particle near-field coupling: Discrete dipole approximation with surface interaction, *Journal of the Optical Society of America A* **27**(10), 2293-2203, 2010.

[25] Loke V.L.Y., Mengüç M.P. and Nieminen T.A., Discrete-dipole approximation with surface interaction: Computational toolbox for MATLAB, *Journal of Quantitative Spectroscopy and Radiative Transfer* **112**, 1711-1725, 2011.

[26] DDA-SI toolbox: http://code.google.com/p/dda-si/. April 8 2013.

[27] Schmehl R., The coupled-dipole method for light scattering from particles on plane surfaces, MS Thesis, Arizona State University, 1994.

CHAPTER 2

PAPER SUBMITTED TO THE *JOURNAL OF QUANTITATIVE SPECTROSCOPY AND RADIATIVE TRANSFER*

The following chapter is submitted to be published in the *Journal of Quantitative Spectroscopy and Radiative Transfer* (JQSRT) as a paper titled, "The discrete dipole approximation with surface interaction for evanescent wave-based characterization of nanostructures on a surface with validation against experimental results." As such, it is to be treated as a stand-alone paper with its own references, sections, and equations. Coauthors of the paper are: Mitchell R. Short,[1] Jean-Michel Geffrin,[2] Redha Abdeddaim,[2] Rodolphe Vaillon[3] and Mathieu Francoeur[1].

[1]*Radiative Energy Transfer Lab, Department of Mechanical Engineering, University of Utah, Salt Lake City, UT 84112, USA*

[2]*Institut Fresnel, CNRS, Université Aix-Marseille, Ecole Centrale Marseille, Campus de St Jérôme, 13013 Marseille, France*

[3]*Université de Lyon, CNRS, INSA-Lyon, UCBL, CETHIL, UMR5008, F-69621, Villeurbanne, France*

2.1 Abstract

The discrete dipole approximation with surface interaction (DDA-SI) is analyzed and expanded for the modeling of far-field scattering by objects on a surface illuminated by an evanescent wave generated by total internal reflection. Far-field scattering predictions via DDA-SI are validated against scaled microwave experimental results for two objects on a surface: a sphere with a diameter of $\lambda/1.92$ and a cube with a side length of $\lambda/1.785$, where λ is the wavelength. A good agreement between experiments and numerical simulations is observed, especially when modified Fresnel reflection coefficients are employed for computing the surface interaction in DDA-SI. Additional programs to calculate the amplitude scattering matrix and Mueller matrix elements via DDA-SI have been created for application to characterization of nanostructures on a surface. For this purpose, the sensitivity of four Mueller matrix elements (M_{11}, M_{12}, M_{21}, and M_{22}) to the particle size, material (gold and silver), shape (sphere and cube), as well as the interparticle spacing, is analyzed. It is found that these elements are sensitive to changes in shape and interparticle spacing, whereas prove insufficient to difference in material and sizes smaller than one-half the wavelength of incident light. Findings show that DDA-SI is a strong predictive model for calculation of far-field scattering, but for characterization purposes other Mueller matrix elements which measure changes in circular polarization must be analyzed.

2.2 Introduction

The need for a real-time, unobtrusive, nanostructure characterization system continues to rise as the use of nanoscale materials increases rapidly. Current imaging methods such as atomic force microscopy (AFM), scanning tunneling microscopy (STM), and scanning electron microscopy (SEM), all provide excellent visual imaging of nanoscale materials, yet are unable to do so without having some effect on the sample. They are also unable to give precise particle characteristics in real-time such as size, arrangement, and composition. One characterization system currently being researched which is expected to provide such characteristics, and in real-time, is the Polarized-Surface-Wave-Scattering System (PSWSS) [1-8]. This framework functions in a noninvasive manner through measuring the far-field scattering profiles (Mueller matrix elements) of nanostructures on a surface illuminated by an evanescent wave generated by total internal reflection (TIR) of a laser beam [8]. The measured scattering profiles, expected to be sensitive to the size, shape, arrangement and composition of the particles, can be employed to characterize nanostructures on a surface via inversion techniques [5-7]. These measurements can also be made in real-time with the only limitation being the speed of the detector. This methodology is promising, yet in order for this system to provide accurate characterization results, a strong theoretical predictive model must also be present.

Prediction of evanescent wave scattering by particles on a surface is a challenging problem. The T-matrix method combined with the normal incidence approximation (NIA) has been used to predict scattering by a sphere on a surface illuminated by a propagating [9,10] and an evanescent [1-4] wave. An exact solution for the problem of

multiple spheres on a surface was also proposed by Mackowski [11]. For characterization purposes, the forward model should be able to accommodate arbitrarily shaped objects on a surface. Numerical approaches such as the null-field method with discrete sources [12] and the finite-difference time-domain method [13] could be employed for that purpose. In this work, evanescent wave scattering by nanostructures on a surface is predicted via the discrete dipole approximation (DDA). DDA is a widely accepted method of solving light scattering by particles from direct propagating illumination. The most well-known application is by Draine and Flatau in the open-source code DDSCAT written in *Fortran* [14,15]. Similarly, ADDA is an open-source *C* software package developed by Yurkin and Hoekstra [16,17]. These codes, however, do not accommodate for evanescent illumination of particles on a surface.

The method being evaluated for the forward model to be used in the PSWSS is the discrete dipole approximation with surface interaction (DDA-SI) developed by Loke et al. [18,19]. DDA-SI was created as an open-source *MATLAB* computational toolbox [20] and is based on the work of Schmehl [21]. DDA-SI has been chosen both for its accuracy as well as its flexibility. DDA-SI is based on discretizing the objects into point electric dipoles, and because calculations are made for each individual dipole, it can accommodate any complex-shape scatterer. This can vary from simple geometries such as cylinders, cubes, and spheres, to more complex agglomerates or arrays of particles. Additionally, DDA-SI can be used both for cases of propagating and evanescent illuminations.

The objective of this work is to use and expand the DDA-SI program package for calculations of far-field scattering (Mueller matrix elements) by objects on a surface

illuminated by an evanescent wave. In the next section, the physical and mathematical description of the problem is provided, and modifications performed in the DDA-SI package are highlighted. The results provided by DDA-SI are then validated against scattering profiles measured at microwave frequencies. Subsequently, the sensitivity of four Mueller matrix elements (M_{11}, M_{12}, M_{21}, M_{22}) is analyzed via DDA-SI for gold and silver nanoparticles illuminated by an evanescent wave generated by TIR of a 632.8 nm laser beam. Lastly, concluding remarks are provided.

2.3 Physical and mathematical description of the problem

2.3.1 Description of the characterization framework

The characterization framework is schematically depicted in Figure 2.1. Nonmagnetic objects (i = 1, 2, …,M), with refractive index n_i, are placed in air (n_2 = 1) on a substrate with refractive index n_1 greater than the refractive index of air. A monochromatic radiation beam of wavelength λ is incident from within the substrate at an angle γ_{inc} measured from the normal to the surface. The incidence angle γ_{inc} is greater than the critical angle γ_{crit} for TIR ($\gamma_{crit} = \sin^{-1}(n_2/n_1)$), such that the propagating beam is totally reflected back in the substrate at an angle $\gamma_r = \gamma_{inc}$ while an evanescent wave, with a field decaying in air, is generated at the substrate-air interface [22]. Particles illuminated by the evanescent field scatter the energy in the far field into directions θ_{scat} = -90° to 90°, as shown in Figure 2.1. The far-field scattering profiles, quantified by the Mueller matrix elements, can be used to retrieve the particle characteristics via an inversion algorithm. Calculation of far-field scattering is performed via DDA-SI, as explained next.

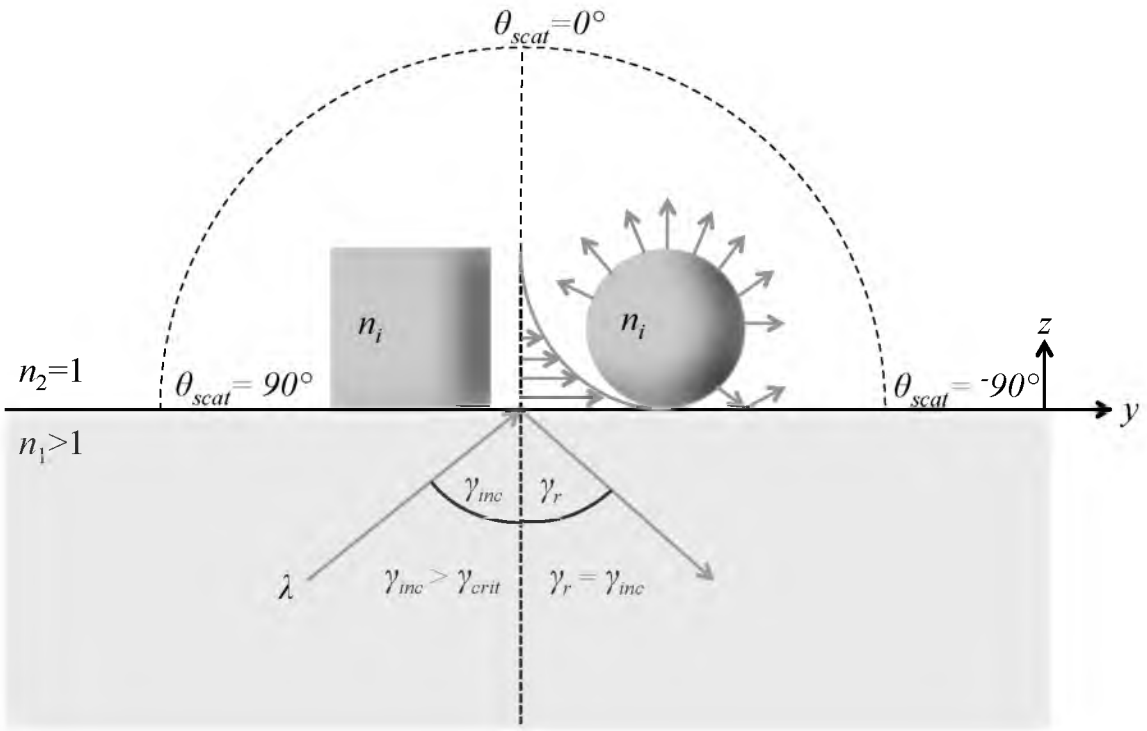

Figure 2.1. Schematic representation of the characterization framework: particles on the substrate are illuminated by an evanescent wave generated by TIR of an external radiation beam.

2.3.2 Calculation of Mueller matrix elements via DDA-SI

The formulation of DDA-SI starts by expressing the total electric field as the sum of incident and scattered electric fields. A system of linear equations is then derived from the total electric field equation by approximating the objects on the surface by N oscillating electric point dipoles on cubical lattice, as shown schematically in Figure 2.2. From discretization into point dipoles, the following system of linear equations is obtained [21]:

$$\left(\overline{\overline{\mathbf{A}}}+\overline{\overline{\mathbf{R}}}\right)\cdot\overline{\mathbf{P}}=\overline{\mathbf{E}}_{inc} \qquad (1)$$

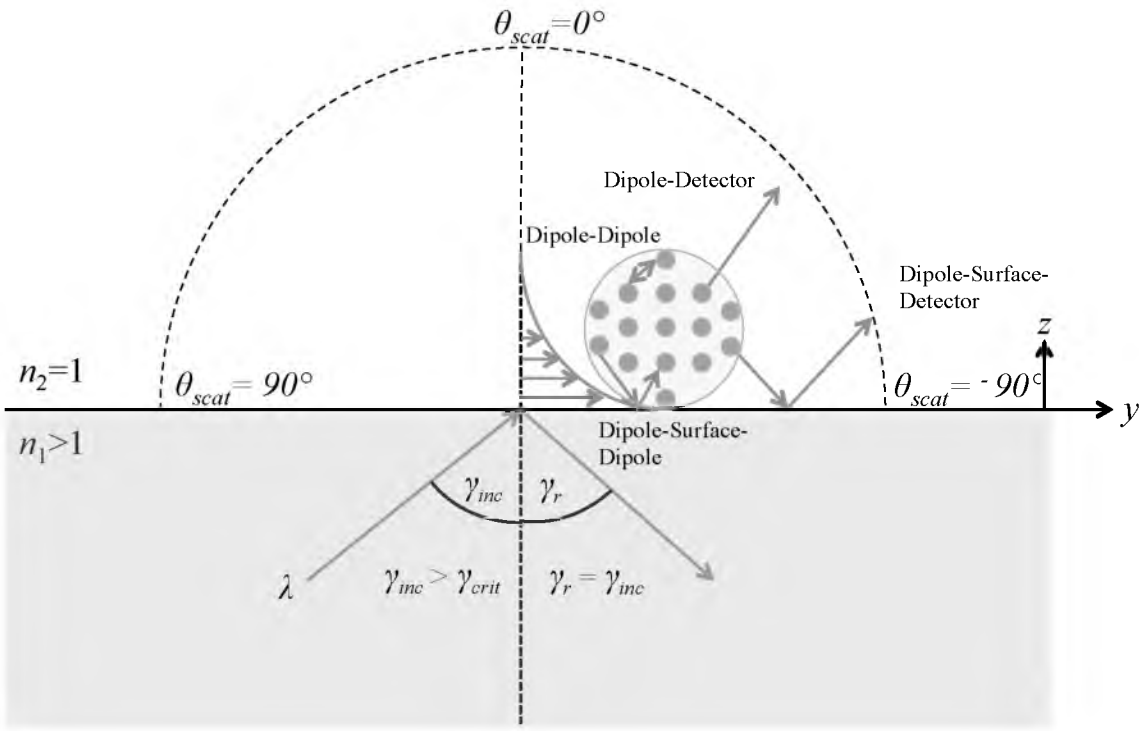

Figure 2.2. Schematic representation of the DDA-SI and the interactions between dipoles and the surface.

where $\overline{\mathbf{E}}_{inc}$ is the $3N$ incident electric field vector due to an external illumination (propagating or evanescent), $\overline{\overline{\mathbf{A}}}$ is the $3N$ by $3N$ interaction matrix that accounts for dipole-dipole interactions (Dipole-Dipole in Figure 2.2), $\overline{\overline{\mathbf{R}}}$ is the $3N$ by $3N$ matrix due to surface interaction, and $\overline{\mathbf{P}}$ is the $3N$ vector containing the N unknown dipole moments $\mathbf{p}_j$ each with x-, y-, and z-components. The dipole moment at a given dipole j is given by $\mathbf{p}_j = \alpha_j \mathbf{E}_j$, where $\mathbf{E}_j$ is the total electric field and α_j is the electric polarizability [19]. In this work, the dipole polarizability is calculated via the lattice dispersion relation (LDR) [19].

As shown in Figure 2.2, the presence of the surface creates additional interactions not present for particles in suspension. The first case is the interaction from a

dipole to the surface and reflected back to another dipole (Dipole-Surface-Dipole in Figure 2.2). This case must be accounted for both in modeling of the incident field and the dipole interactions (via the surface interaction matrix $\overline{\overline{\mathbf{R}}}$). Second, a calculation must be made for the reflected portion of the scattering profile from a dipole to the surface and to the detector (Dipole-Surface-Detector in Figure 2.2); this is accounted for when computing the scattered fields. Both of these cases deal with a reflection off a plane surface and are calculated based on image theory using the Fresnel reflection coefficients [21]. Note that more in-depth mathematical details of the DDA-SI can be found in Refs. [18,19,21] and are not repeated here.

Once the dipole moments have been calculated from Eq. (1), various quantities such as the absorption and scattering cross-sections can be considered. In this paper, the change of intensity and linear polarization after scattering are analyzed via the Mueller matrix elements M_{11}, M_{12}, M_{21} and M_{22}. Two main reasons justify this choice. First, experimental measurement of the four aforementioned elements is relatively simple. The experiments only require two linear polarizers: one located before the sample to prepolarize the radiation beam, and one located after the sample to polarize the scattered field [8,23]. The four elements M_{11}, M_{12}, M_{21} and M_{22} are retrieved by performing four independent experiments using different orientations for the linear polarizers (TE-TE, TE-TM, TM-TM and TM-TE). Second, the described experimental technique is independent of the form of the Mueller matrix of the sample. For instance, the characterization framework described by Mengüç and Manickavasagam [24] is based on the assumption that the Mueller matrix of the sample reduces to six independent and nonzero elements for a symmetric cloud of randomly oriented particles. No such

assumption is necessary for measuring M_{11}, M_{12}, M_{21} and M_{22} via two linear polarizers [8].

Using DDA-SI, the four Mueller matrix elements of interest are calculated as follows [23]:

$$M_{11} = \frac{1}{2}\left(|S_1|^2 + |S_2|^2 + |S_3|^2 + |S_4|^2\right) \tag{2a}$$

$$M_{12} = \frac{1}{2}\left(|S_2|^2 - |S_1|^2 + |S_4|^2 - |S_3|^2\right) / M_{11} \tag{2b}$$

$$M_{21} = \frac{1}{2}\left(|S_2|^2 - |S_1|^2 - |S_4|^2 + |S_3|^2\right) / M_{11} \tag{2c}$$

$$M_{22} = \frac{1}{2}\left(|S_2|^2 + |S_1|^2 - |S_4|^2 - |S_3|^2\right) / M_{11} \tag{2d}$$

where S_j (j = 1 to 4) are the amplitude scattering matrix elements. These elements are calculated from the dipole moments via the following relations [21]:

$$S_1 = \frac{-ik_0^3}{4\pi\varepsilon_0}\sum_{j=1}^{N}\left\{e^{-i\mathbf{k}_{sca}\cdot\mathbf{r}_j} + r^{TE}e^{-i\mathbf{k}_{sca}\cdot\mathbf{r}_{1,j}}\right\}\mathbf{p}_j^{(2)}\cdot\mathbf{e}_2 \tag{3a}$$

$$S_2 = \frac{-ik_0^3}{4\pi\varepsilon_0}\sum_{j=1}^{N}\left\{e^{-i\mathbf{k}_{sca}\cdot\mathbf{r}_j} + r^{TM}e^{-i\mathbf{k}_{sca}\cdot\mathbf{r}_{1,j}}\right\}\mathbf{p}_j^{(1)}\cdot\mathbf{e}_1 \tag{3b}$$

$$S_3 = \frac{-ik_0^3}{4\pi\varepsilon_0}\sum_{j=1}^{N}\left\{e^{-i\mathbf{k}_{sca}\cdot\mathbf{r}_j} + r^{TM}e^{-i\mathbf{k}_{sca}\cdot\mathbf{r}_{1,j}}\right\}\mathbf{p}_j^{(2)}\cdot\mathbf{e}_1 \tag{3c}$$

$$S_4 = \frac{-ik_0^3}{4\pi\varepsilon_0}\sum_{j=1}^{N}\left\{e^{-i\mathbf{k}_{sca}\cdot\mathbf{r}_j} + r^{TE}e^{-i\mathbf{k}_{sca}\cdot\mathbf{r}_{1,j}}\right\}\mathbf{p}_j^{(1)}\cdot\mathbf{e}_2 \tag{3d}$$

where k_0 is the magnitude of the wavevector in air, $\mathbf{e}_1$ and $\mathbf{e}_2$ are unit vectors oriented along the TM and TE polarization states, while $\mathbf{p}_j^{(1)}$ and $\mathbf{p}_j^{(2)}$ represent the dipole moments calculated from a TM incident field and a TE incident field, respectively. In Eqs. (3a) to (3d), $\mathbf{r}_j$ and $\mathbf{k}_{sca}$ are respectively the coordinates of dipole j and the scattered wavevector; the same explanations hold for $\mathbf{r}_{I,j}$ and $\mathbf{k}_{I,sca}$, except that these variables are associated with the image dipole [21]. The Fresnel reflection coefficients in TM and TE polarizations are calculated as follows for nonmagnetic materials [21,22]:

$$r^{TM} = \frac{k_{z2}\varepsilon_1 - k_{z1}}{k_{z2}\varepsilon_1 + k_{z1}} \tag{4a}$$

$$r^{TE} = \frac{k_{z2} - k_{z1}}{k_{z2} + k_{z1}} \tag{4b}$$

where,

$$k_{z2} = k_0 \cos\theta \tag{5a}$$

$$k_{z1} = k_0 \sqrt{n_1^2 - \sin^2\theta} \tag{5b}$$

Note that Eqs. (4) and (5) assume that medium 2 is air.

Supplementary details about the *MATLAB* implementation of DDA-SI and the modifications performed in the package are summarized next.

2.3.3 Details of DDA-SI implementation

The core of DDA-SI revolves around solving the system of equations in Eq. (1) for the dipole moment vector $\overline{\mathbf{P}}$ that contains N dipole moments $\mathbf{p}_j$. This can be done

using one of the many iterative solvers available in *MATLAB*; the quasi-minimal residual method, '*qmr.m*', was used for the bulk of this work, but the minimum residual method, '*minres.m*', and general minimum residual method, '*gmres.m*', are also recommended in the DDA-SI User Manual [25]. Once the dipole moments have been found, they can be used to calculate the various necessary outputs.

Calculation of the Mueller matrix elements and amplitude scattering matrix had not previously been implemented in the DDA-SI package. As such, two new programs were added. Also, in order to calculate the four amplitude scattering elements, a new program had to be written which could make calculations for both a TM-polarized incident wave and a TE-polarized incident wave. This program was constructed on the same principles as outlined above to calculate the dipole moments and scattered field, but was repeated twice for the two different incident field polarizations. First, the program runs through using a TM-polarized incident wave to calculate and store the S_2 and S_4 elements, and then restarts using the same parameters but a TE-polarized incident wave to calculate and store the S_1 and S_3 elements. Once all four amplitude scattering matrix elements are calculated, they are used in the Mueller matrix program to calculate the sixteen Mueller matrix elements, or in this case, the four particular elements of interest.

Finally, a change was made in the calculation of the Fresnel reflection coefficients. The original method of calculating the Fresnel coefficients was modified in order to improve the accuracy of the numerical predictions. In the original version of DDA-SI, the Fresnel coefficients were computed using the NIA, such that r^{TM} and r^{TE} were calculated only once at the normal angle $\theta = 0^{\circ}$. Using the NIA, these two values were used for all subsequent calculations involving the variables r^{TM} and r^{TE}. In the

results which were verified and published previously using DDA-SI [18,19], the angle of incidence was normal to the surface from above the scatterer; thus, a single calculation provided a quasi-average for the range of the detector-space. Although the results still compared well for that scattering profile, the farther from normal the detector angle, the less accurate this approximation becomes. The reflection coefficients are a key variable in the calculation of the scattered field with a surface present; they impact the calculation of the dipole-surface-dipole interaction as well as the dipole-surface-detector scattered field. A more accurate calculation of Fresnel coefficient values gives a more consistently accurate scattered field calculation. Furthermore, in the case of evanescent illumination, the angle of incidence is no longer indicative of the field at the dipoles. In order to resolve this uncertainty, a modification was made in the '*E_sca_SI.m*' subroutine [19]. With this modification, the Fresnel coefficients are recalculated for each dipole at the actual reflection angle.

DDA-SI is employed to analyze the sensitivity of M_{11}, M_{12}, M_{21}, and M_{22} for gold and silver nanoparticles on surface illuminated by an evanescent wave. This analysis will assist in determining whether or not the four aforementioned Mueller matrix elements are sufficient for characterization purpose. Before performing this study, DDA-SI is validated in the next section against experimental results obtained at microwave frequencies.

2.4 Validation of DDA-SI against microwave analog experiments

DDA-SI predictions of light scattering by particles on a surface illuminated by an evanescent wave are validated using scaled microwave analog measurements. Microwave

analog experiments have been reported for particles in suspension [26-30], but to the best of our knowledge, evanescent wave scattering by particles on a surface at microwave frequencies has never been discussed in the literature. The details of the experimental apparatus are not provided here, but are described along with the main principles in the form of a patent application [31].

Experimental measurements were made for cubes and spheres with size parameters of $\lambda/2.5$ to $\lambda/0.83$ (frequencies between 4 and 6 GHz). In this spectral band, the prism used to achieve the TIR condition is made of polyamide (PA6). It has a measured refractive index of $n_1 = 1.7030 + i0.0147$, such that the critical angle for TIR, γ_{crit}, is 36°. In Figure 2.3, a polyethylene (PE) cube, with refractive index $n_i = 1.533 + i0$ and a side length of $\lambda/1.785$, is illuminated by a TE-polarized wave (frequency of 4.2 GHz) from an incident angle of 43.5°. Similar results are shown in Figure 2.4, except that the scatterer is an index-matching PA6 sphere with a diameter of $\lambda/1.92$, illuminated by a TE-polarized wave (frequency of 5.2 GHz) from an incident angle of 37.5°. In both figures, far-field scattering profiles are calculated by $20\log\left|\mathbf{E}_{sca}^{TE}\right|$; thus, the scale may appear linear but is in fact logarithmic. The experimental far-field scattering profiles are reported as a function of the angle θ and compared against DDA-SI predictions. The scattered field in TE polarization is calculated by DDA-SI as follows [21]:

$$\mathbf{E}_{sca}^{TE}(\mathbf{r}) = k_0^2 \frac{e^{ik_0 r}}{4\pi r} \sum_{j=1}^{N} \left\{ e^{-i\mathbf{k}_{sca}\cdot\mathbf{r}_j} (\mathbf{p}_j \cdot \mathbf{e}_2)\mathbf{e}_2 + e^{-i\mathbf{k}_{1,sca}\cdot\mathbf{r}_j} r^{TE} (\mathbf{p}_j \cdot \mathbf{e}_2)\mathbf{e}_2 \right\} \tag{6}$$

where all variables have been defined in section 2.3.2.

The impact of the change made in the Fresnel reflection coefficients can be seen in Figure 2.3, where the dashed line is using the original reflection coefficient calculation and the solid line is using the new method described in section 2.4. The repeatability of the experimental results is also shown through two separate, but consistent measurements. The results and simulations compared well before the Fresnel reflection coefficient change, but even better after. The improvement is most noticeable at scattering angles closer to the experimental limits of -75° and 75°, which is to be expected as they are farthest from the normal axis. Consequently, the modified Fresnel reflection coefficients are employed in all simulations reported in this paper.

For the case of a PA6 sphere, the microwave analog experimental results and DDA-SI are also in good agreement. Two DDA-SI curves are shown in Figure 2.4 for two angles of incidence: the dashed line for the measured incidence angle of 37.5° and the solid line for 36.5°. Figure 2.4 suggests that the scattering profile is generally insensitive to a small perturbation of the incident angle, except at the dip located at an angle of 40°. The comparison between DDA-SI and experiments also reveal that simulations using an incident angle of 36.5° match the experimental scattering profile better than the measured incident angle of 37.5°. This slight inconsistency suggests possible imprecisions associated with measuring the incident angle in the experimental apparatus, though within the expected experimental uncertainty.

Utilizing the dipole configurations provided in the DDA-SI toolbox [20], 512 dipoles were sufficient to provide a converged solution for the case of the PE cube, and 912 dipoles were used in the case of the PA6 sphere. The number of dipoles necessary for a converged solution is dependent on the permittivity, shape, quantity, and size of

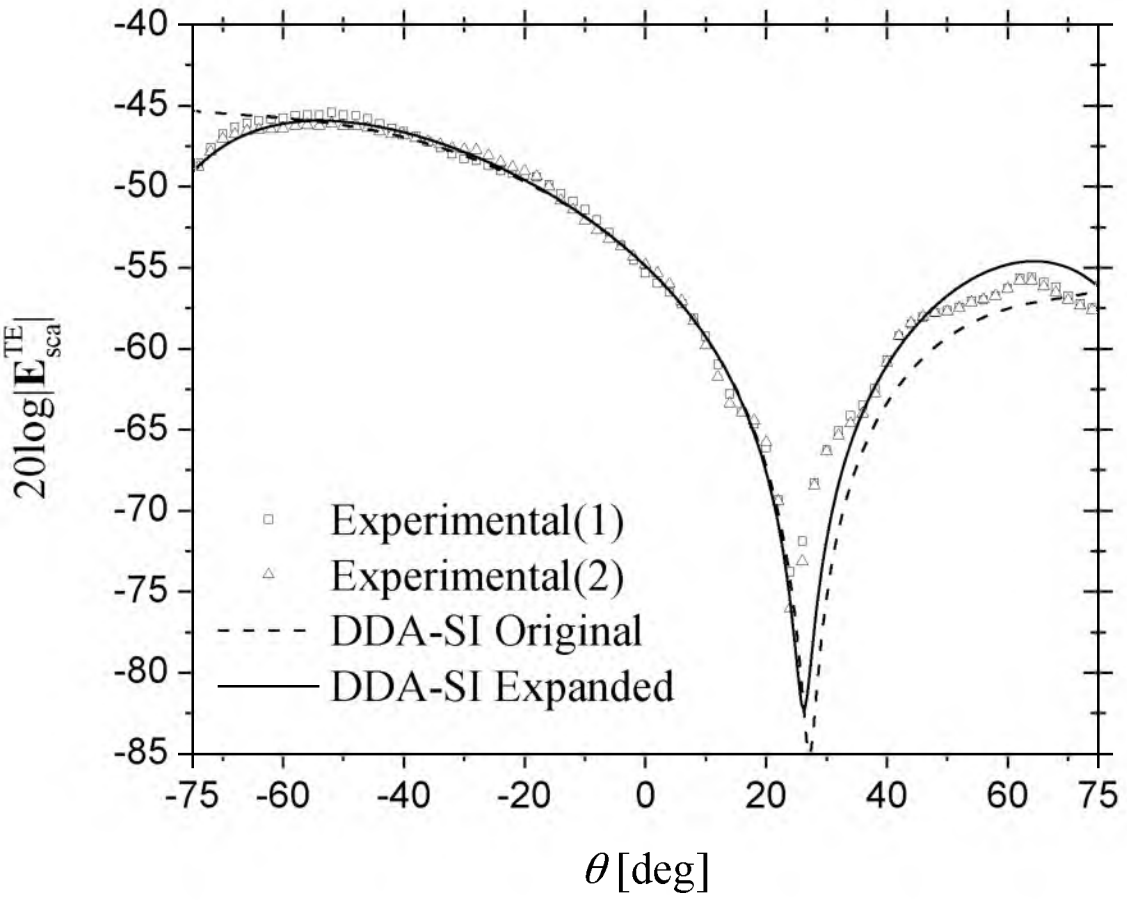

Figure 2.3. Far-field scattering by a PE cube (λ/1.785 side length) illuminated by an evanescent wave: comparison between experimental results and DDA-SI predictions before and after modifications of the Fresnel reflection coefficients.

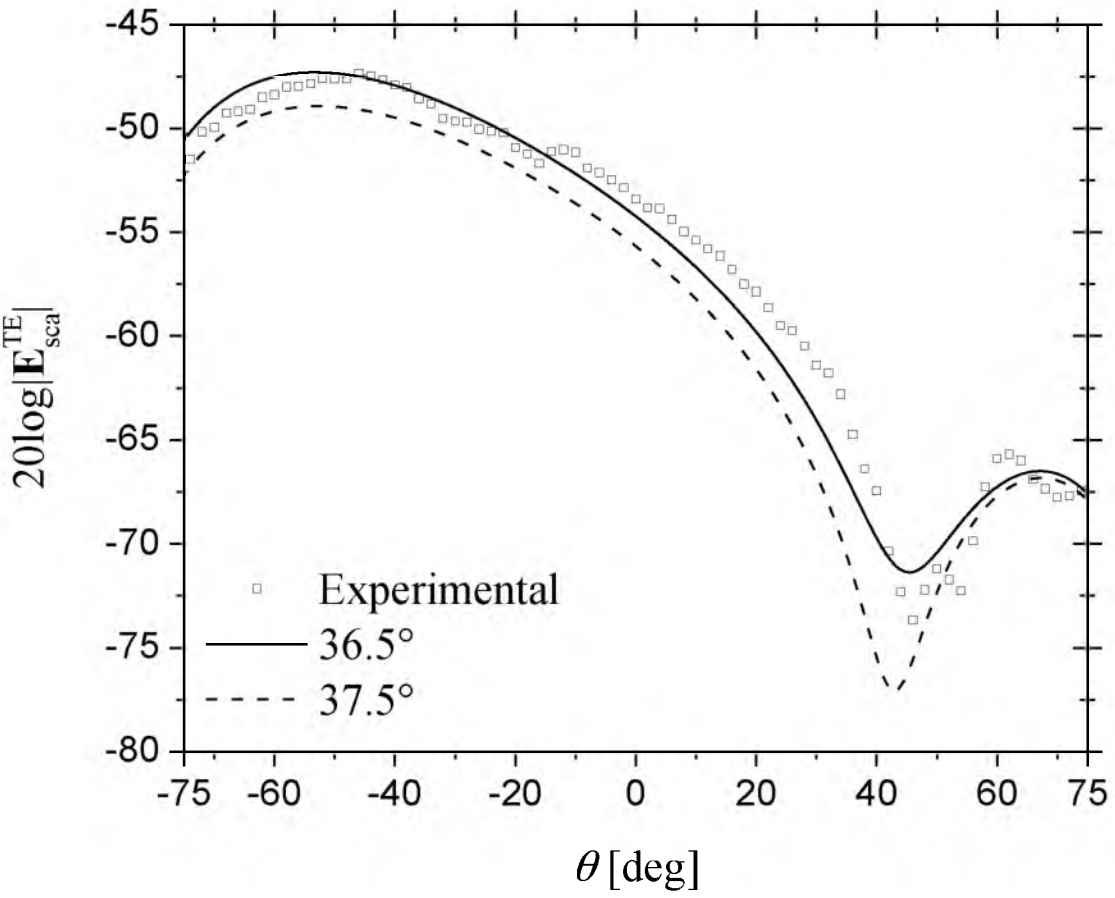

Figure 2.4. Far-field scattering by a PA6 sphere (λ/1.92 diameter) illuminated by an evanescent wave: comparison between experimental results and DDA-SI predictions with modified Fresnel reflection coefficients.

object(s), as well as the wavelength and angle of the incident beam [32,33]. The comparison between DDA-SI and experimental results of far-field scattering profile is promising. Further experiments involving multiple scatterers of various shapes, sizes, and permittivities are however required for a complete validation of DDA-SI. Nevertheless, Figures 2.3 and 2.4 provide confidence about the accuracy of DDA-SI, and suggest that this numerical approach can be employed as a forward model for application to the PSWSS and can be used to establish calibration experiments for the system.

2.5 Nanostructure sensitivity analysis

The PSWSS will be utilized for particles of varying size, shape, material, and arrangement. In order to establish experiments and a proper calibration of the system, DDA-SI is used hereafter to analyze the sensitivity of the measurements by modeling variances in these aforementioned parameters. Specifically, the sensitivity of the Mueller matrix elements M_{11}, M_{12}, M_{21}, and M_{22} to the particle size, material, and shape, as well as to the interparticle spacing is analyzed. In all simulations, particles deposited on a sapphire substrate are illuminated by an evanescent wave generated by TIR of a 632.8 nm radiation beam. At this wavelength, the refractive indices of sapphire, gold (Au), and silver (Ag) are $n_1 = 1.7659$, $n_{Au} = 0.1846 + i3.4262$, and $n_{Ag} = 0.0564 + i4.2721$, respectively [34]. The incident angle at the sapphire-air interface, γ_{inc}, is 36° (the critical angle for TIR is 34.5°). Note that all profiles are reported for scattering angles between -75° and 75°, which are measurable via the PSWSS.

Figures 2.5(a) to 2.5(d) show the Mueller matrix elements for gold particles with diameters of 50 nm, 100 nm, 200 nm, and 400 nm, or a size parameter range of $\lambda/12.656$

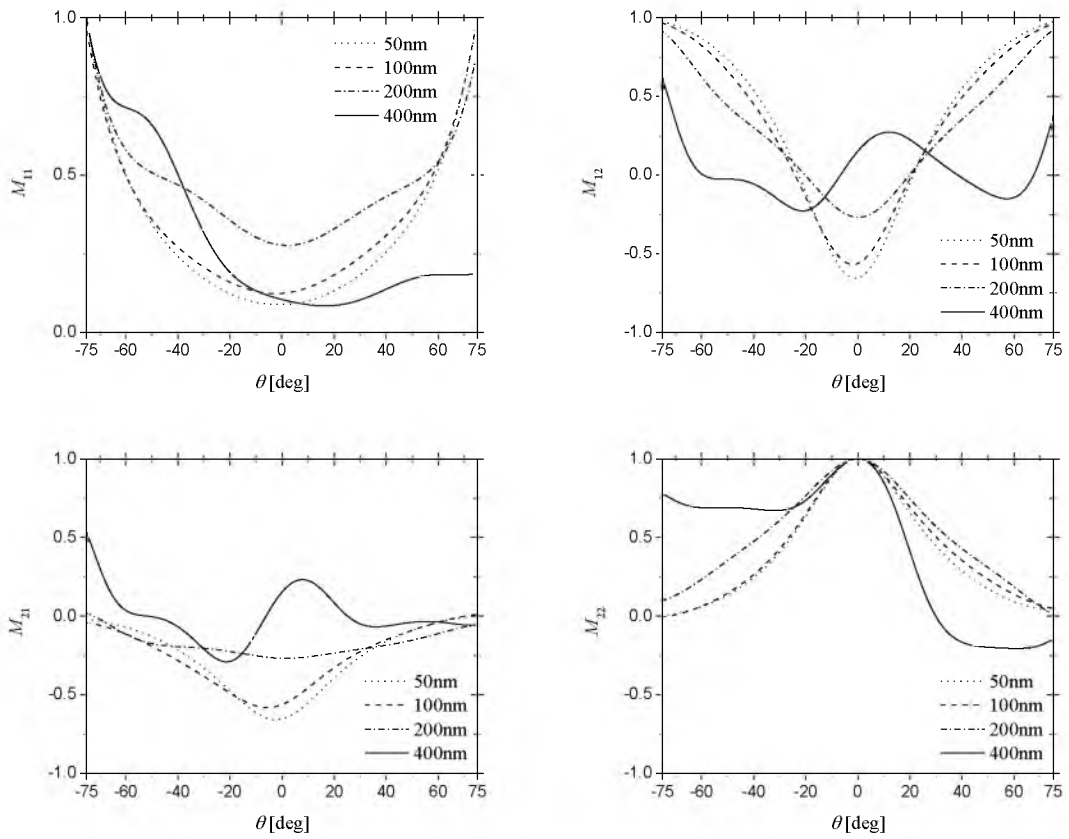

Figure 2.5. Mueller matrix elements for gold spheres with diameters of 50 nm, 100 nm, 200 nm, and 400 nm: (a) M_{11}, (b) M_{12}, (c) M_{21}, (d) M_{22}.

to $\lambda/1.582$. Because of the high permittivity of silver and gold, a larger number of dipoles is necessary for a converged solution, as is common for DDA style approach [35]. Similarly, some Mueller elements, often M_{12}, do not converge as readily as others. For the smaller objects of 50 nm and 100 nm, 912 dipoles was still sufficient. For 200 nm spheres, 1472 dipoles were required, and once the size parameter was larger than $\lambda/2$ at 400 nm, the number dipoles necessary for convergence reached 3112.

From Figure 2.5, it is clear that measuring the scattered intensity may not be sufficient for distinguishing the particle size, since M_{11} profiles at smaller sizes have

essentially the same shape. As the particle size becomes larger than $\lambda/2$, slight fluctuations in M_{11} occur due to development of another resonance mode. However, this slight change of the profile is unlikely to be sufficient for characterizing the particle size. Additionally, for particle size of 50 and 100 nm, the M_{12}, M_{21}, and M_{22} profiles are very similar to each other. For such small particles, it seems necessary to measure the change in circular polarization for distinguishing the particle size. Note that similar results have been obtained for silver (not shown).

The sensitivity of the four Mueller matrix elements to the material is analyzed in Figures 2.6(a) to 2.6(d), where 400 nm diameter gold and silver particles are considered. Once again, at 400 nm, 3112 dipoles were necessary for a converged solution. Through the analysis of the four Mueller matrix elements for various sphere diameters, it was observed that the difference between gold and silver is only slightly apparent for particle size beyond $\lambda/2$, and not at all apparent for smaller particles. Figures 2.6(a) to 2.6(d) suggest that measuring the change of intensity and linear polarization after scattering is insufficient in order to characterize relatively similar materials such as gold and silver. Further analysis of change in circular polarization may be necessary via other Mueller matrix elements such as M_{33}, thus making the characterization procedure more tedious from an experimental viewpoint.

The sensitivity of the scattering profiles to the shape of the scatterers with the same size parameter is studied in Figures 2.7(a) to 2.7(d), where gold spheres (200 nm diameter) and gold cubes (200 nm side length) are considered. A converged solution for the cubes was still found with 512 dipoles, whereas the spheres required a higher number at 1472. By varying the shape of objects, while maintaining the same material and size

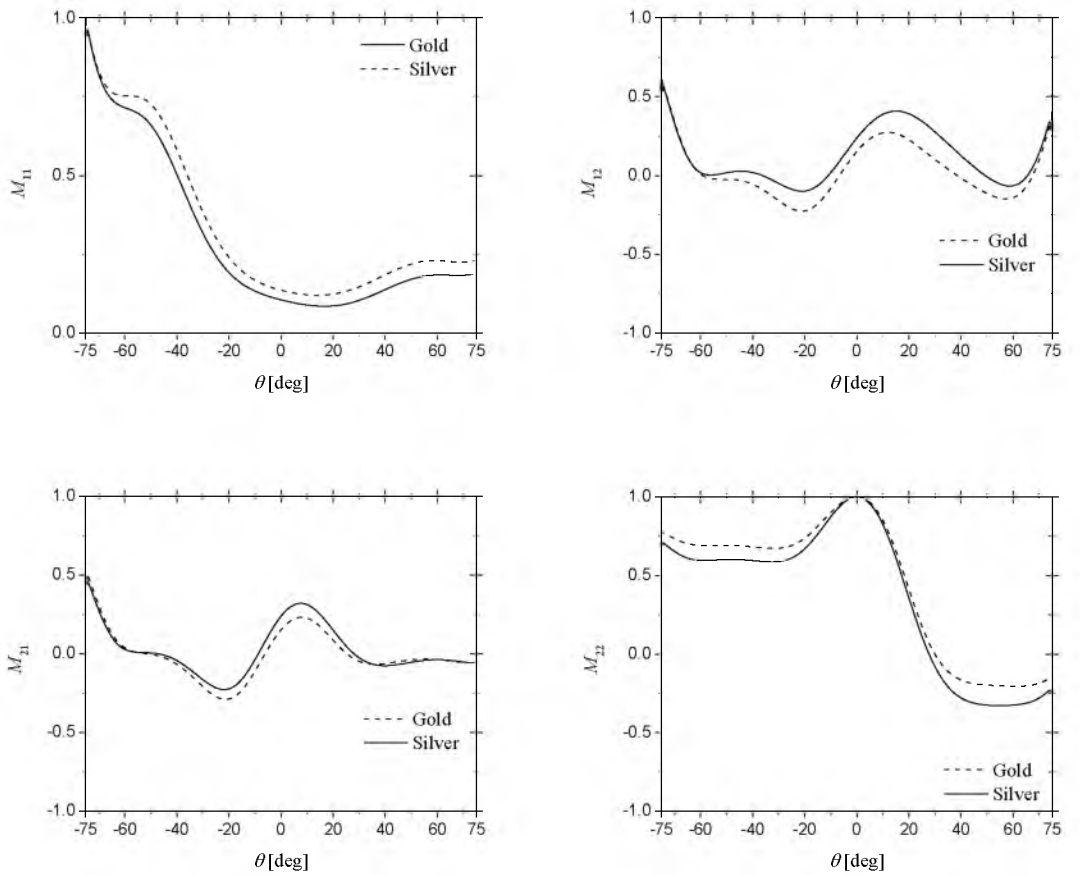

Figure 2.6. Mueller matrix elements for gold and silver spheres with diameter of 400 nm: (a) M_{11}, (b) M_{12}, (c) M_{21}, (d) M_{22}.

parameter, different resonances become apparent. The three elements M_{12}, M_{21}, and M_{22} are quite sensitive to the particle shape, thus suggesting that the change of linear polarization after scattering is sufficient for characterizing the shape. Similar results are found for a comparison between a cube of 200 nm and a sphere of equal volume (diameter of 248 nm) though at smaller volumes, the two become less distinguishable. This suggests a lower limit for shape characterization of a size parameter of about $\lambda/3$. Similar outcomes are expected for comparison between single particles and particle agglomerates. The same results have also been obtained for silver and are not shown.

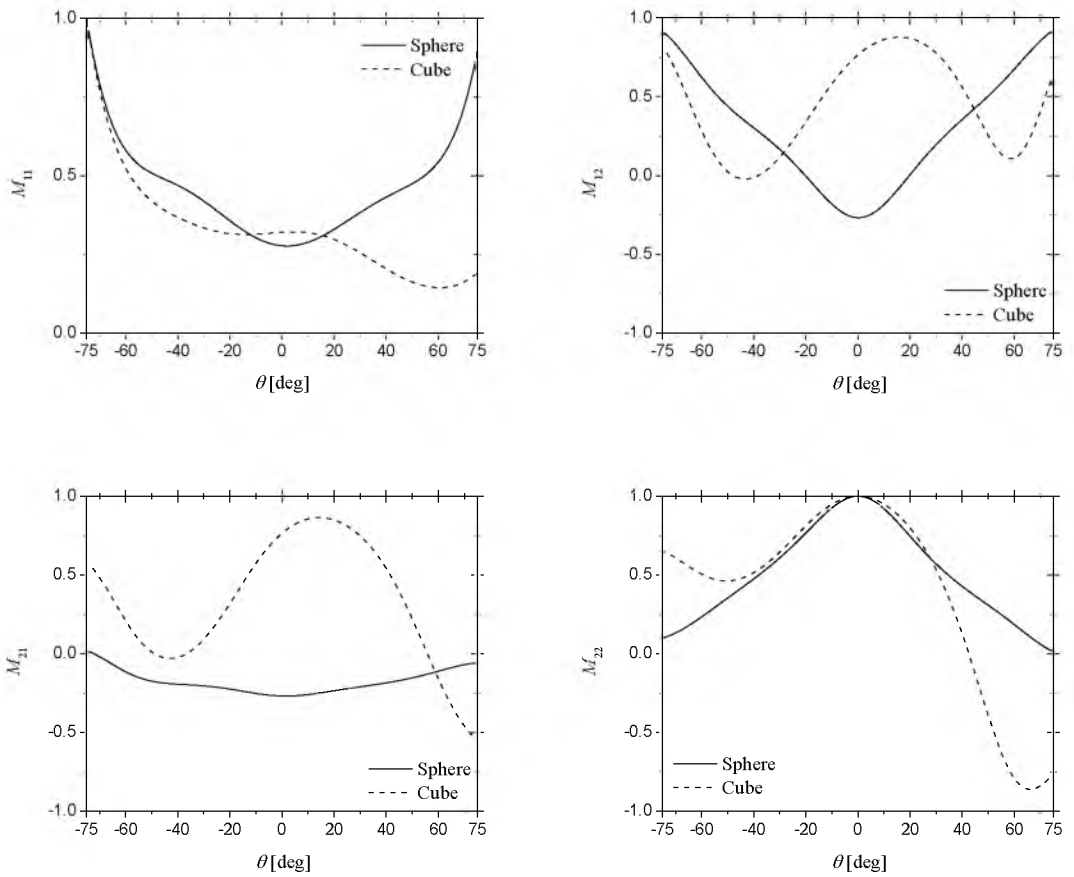

Figure 2.7. Mueller matrix elements for gold spheres (200 nm diameters) and gold cubes (200 nm side lengths): (a) M_{11}, (b) M_{12}, (c) M_{21}, (d) M_{22}.

Finally, the sensitivity of the Mueller matrix elements is analyzed for four like-objects (cubes) equidistant from one-another. DDA-SI simulations for arrangements of four gold cubes (200 nm side length) of varying separation distance (300 nm, 1λ, and 2λ), compared to a single 200 nm gold cube, results are shown in Figures 2.8(a) to 2.8(d) using 512 dipoles per cube. Different interparticle distances lead to different resonance modes in the scattering profiles. The scattered intensity (M_{11}) is quite sensitive to the particle configuration, and could thus be employed for characterizing this parameter. As the interparticle distance is increased, the expectation is to develop independent

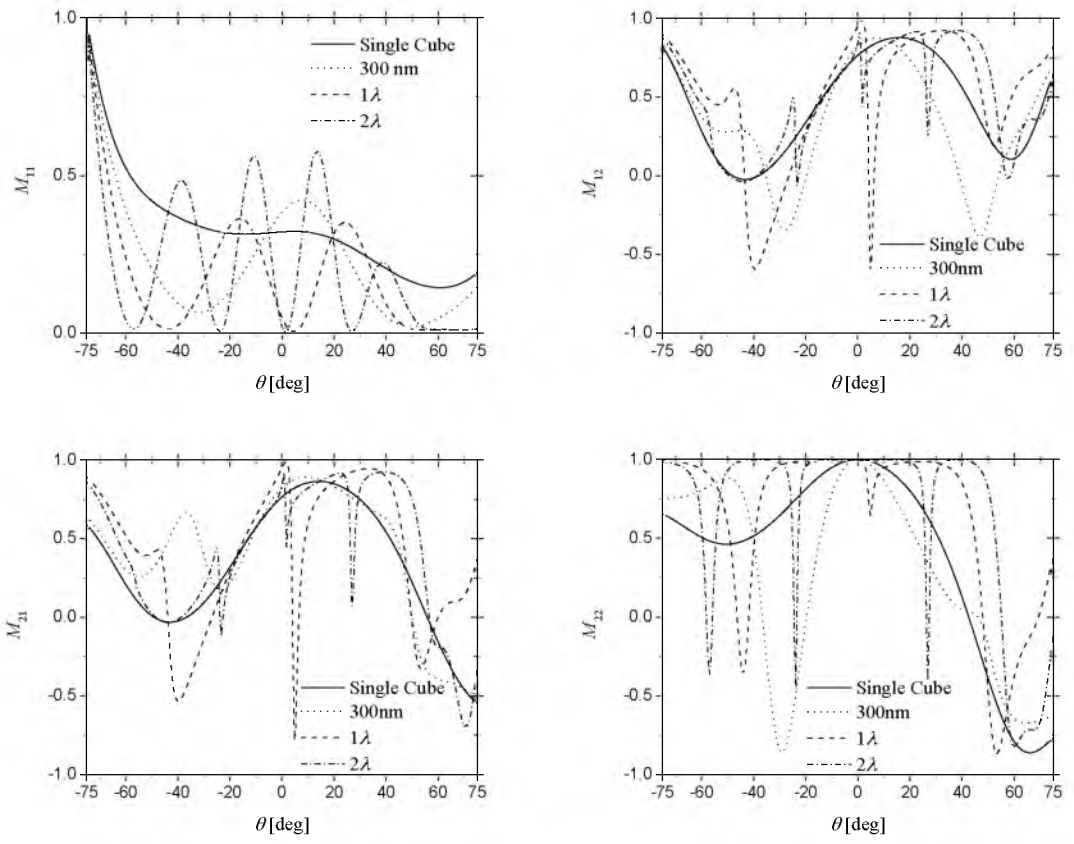

Figure 2.8. Mueller matrix elements for arrangements of four gold cubes (200 nm side length) of varying distance apart, compared to a single 200 nm gold cube: (a) M_{11}, (b) M_{12}, (c) M_{21}, (d) M_{22}.

scattering, i.e., the same profiles as a single cube. As the spacing is increased to a very large distance such as 6λ (not shown), DDA-SI resembles the curve of a single cube; however, there is a very large amount of noise. The beginning stages of this can be seen in the general shape of the 2λ spacing curve: a tendency to look similar to the single cube case but with more oscillations. For this reason, it has been concluded that more evaluation will need to be done using the upcoming experiments for a proper "cut-off" between dependent and independent scattering.

2.6 Conclusions

The discrete dipole approximation with surface interaction (DDA-SI) has been analyzed as a potential forward model for noninvasive, real-time characterization of nanostructures on a surface using scattered evanescent waves. DDA-SI has been compared against microwave analog experimental results for the cases of a sphere and a cube. A good agreement between experiments and predictions has been observed, especially after performing modifications in the Fresnel reflection coefficients in DDA-SI. The DDA-SI has been expanded to accommodate the calculation of the Mueller matrix elements, and has been employed to evaluate the sensitivity of M_{11}, M_{12}, M_{21}, and M_{22} to the particle size, material (gold and silver), and shape (sphere and cube), as well as to the interparticle spacing. Results have shown that measuring the change of intensity and linear polarization of scattered evanescent waves is sufficient for characterizing particle shape and separation distance. However, characterizing nanoparticle size smaller than $\lambda/2$ and distinguishing gold from silver via the four aforementioned Mueller matrix elements seems impossible. As such, it will be necessary to measure the change of circular polarization to infer these parameters.

For future research efforts, a more extensive validation of DDA-SI will be performed via microwave experiments on multiple scatterers of various shapes, sizes, and permittivities. Additionally, DDA-SI will be compared against Mueller matrix elements measured in the visible spectrum using the PSWSS.

2.7 Acknowledgements

This work was partially supported by the US Army Research Office under Grant No. W911NF-12-1-0422 Mod. 1 and by the Institut Carnot STAR (France).

2.8 References

[1] Videen G., Aslan M.M. and Mengüç M.P., Characterization of metallic nano-particles via surface wave scattering: A. Theoretical framework and formulation, *Journal of Quantitative Spectroscopy and Radiative Transfer* **93**, 195-206, 2005.

[2] Aslan M.M., Mengüç M.P. and Videen G., Characterization of metallic nano-particles via surface wave scattering: B. Physical concept and numerical experiments, *Journal of Quantitative Spectroscopy and Radiative Transfer* **93**, 207-217, 2005.

[3] Venkata P.G., Aslan M.M., Mengüç M.P. and Videen G., Surface plasmon scattering patterns of gold nanoparticles and 2D agglomerates, *ASME Journal of Heat Transfer* **129**, 60-70, 2007.

[4] Francoeur M., Venkata P.G. and Mengüç M.P., Sensitivity analysis for characterization of gold nanoparticles and agglomerates via surface Plasmon scattering patterns, *Journal of Quantitative Spectroscopy and Radiative Transfer* **106**, 44-55, 2007.

[5] Charnigo R., Francoeur M., Mengüç M.P., Brock A., Leichter M. and Srinivasan C., Derivatives of scattering profiles: tools for nanoparticle characterization, *Journal of the Optical Society of America A* **24**, 2578-2589, 2007.

[6] Charnigo R., Francoeur M., Kenkel P., Mengüç M.P., Hall B. and Srinivasan C., Estimating quantitative features of nanoparticles using multiple derivatives of scattering profiles, *Journal of Quantitative Spectroscopy and Radiative Transfer* **112**, 1369-1382, 2011.

[7] Charnigo R., Francoeur M., Kenkel P., Mengüç M.P., Hall B. and Srinivasan C., Credible intervals for nanoparticle characteristics, *Journal of Quantitative Spectroscopy and Radiative Transfer* **113**, 182-193, 2011.

[8] Francoeur M., Near-Field Radiative Transfer: Thermal Radiation, Thermophotovoltaic Power Generation and Optical Characterization, PhD Dissertation, University of Kentucky, 2010.

[9] Videen G., Light scattering from a sphere on or near a surface, *Journal of the Optical Society of America A* **8**, 483-499, 1991.

[10] Videen G., Turner M.G., Iafelice V.J., Bickel W.S. and Wolfe W.L., Scattering from a sphere near a surface, *Journal of the Optical Society of America A* **10**, 118-126, 1993.

[11] Mackowski D.W., Exact solution for the scattering and absorption properties of sphere clusters on a plane surface, *Journal of Quantitative Spectroscopy and Radiative Transfer* **109**, 770-788, 2008.

[12] A. Doicu, T. Wriedt and Y.A. Eremin, *Light Scattering by Systems of Particles*, Springer, 2006.

[13] Muller J., Parent G., Jeandel G. and Lacroix D., Finite-difference time-domain and near-field-to-far-field transformation in the spectral domain: Application to scattering objects with complex shapes in the vicinity of a semi-infinite dielectric medium, *Journal of the Optical Society of America A* **28**, 868-878, 2011.

[14] Flatau P.J. and Draine B.T., Discrete dipole approximation for scattering calculations, *Journal of the Optical Society of America A* **11**, 1491-1499, 1994.

[15] Draine, B.T. and Flatau, P.J., User guide to the discrete dipole approximation code DDSCAT 7.2, http://arXiv.org/abs/1202.3424, 2012.

[16] Hoekstra A.G. and Yurkin M.A., The discrete-dipole-approximation code ADDA: Capabilities and known limitations, *Journal of Quantitative Spectroscopy and Radiative Transfer* **112**, 2234-2247, 2011.

[17] Yurkin M.A. and Hoekstra A.G., The discrete dipole approximation: An overview and recent developments, *Journal of Quantitative Spectroscopy and Radiative Transfer* **106**, 558-589, 2007.

[18] Loke V.L.Y. and Mengüç M.P., Surface waves and atomic force microscope probe-particle near-field coupling: Discrete dipole approximation with surface interaction, *Journal of the Optical Society of America A* **27**(10), 2293-2203, 2010.

[19] Loke V.L.Y., Mengüç M.P. and Nieminen T.A., Discrete-dipole approximation with surface interaction: Computational toolbox for MATLAB, *Journal of Quantitative Spectroscopy and Radiative Transfer* **112**, 1711-1725, 2011.

[20] DDA-SI toolbox: http://code.google.com/p/dda-si/. April 8 2013.

[21] Schmehl R., The coupled-dipole method for light scattering from particles on plane surfaces, MS Thesis, Arizona State University, 1994.

[22] Novotny L. and Hecht B., *Principles of Nano-Optics*, Cambridge University Press, New York, 2006.

[23] Bohren C.F. and Huffman D.R., *Absorption and Scattering of Light by Small Particles*, Wiley, New York, 1983.

[24] Mengüç M.P. and Manickavasagam S., Characterization of size and structure of agglomerates and inhomogeneous particles via polarized light, *International Journal of Engineering Science* **36**, 1569-1593, 1998.

[25] Loke V., Discrete Dipole Approximation with Surface Interaction DDA-SI for MATLAB - User Guide: http://code.google.com/p/dda-si/. April 8 2013.

[26] Sabouroux P., Stout B., Geffrin J.-M., Eyraud C., Ayranci I., Vaillon R. and Selçuk N., Amplitude and phase of light scattered by micro-scale aggregates of dielectric spheres: Comparison between theory and microwave analogy experiments, *Journal of Quantitative Spectroscopy and Radiative Transfer* **103**, 156-167, 2007.

[27] Merchiers O., Geffrin J.-M., Vaillon R., Sabouroux P. and Lacroix B., Microwave analog to light scattering measurements on a fully characterized complex aggregate, *Applied Physics Letters* **94**, 181107, 2009.

[28] Merchiers O., Eyraud C., Geffrin J.-M., Vaillon R., Stout B., Sabouroux P. and Lacroix B., Microwave measurements of the full amplitude scattering matrix of a complex aggregate: a database of the assessment of light scattering codes, *Optics Express* **18**, 2056-2075, 2010.

[29] Vaillon R., Geffrin J.-M., Eyraud C., Merchiers O., Sabouroux P. and Lacroix B., A new implementation of a microwave analog to light scattering measurement device, *Journal of Quantitative Spectroscopy and Radiative Transfer* **112**, 1753-1760, 2011

[30] Gustafson BÅS., Scaled analogue experiments in electromagnetic scattering. In: Kokhanovsky AA, editor. Light scattering reviews 4—single light scattering and radiative transfer. Berlin: Springer; 3-30, 2009.

[31] Vaillon R., Lacroix B., Geffrin J.-M., and Abdeddaim R., Dispositif d'imagerie en champ proche et lointain dans le domaine des micro-ondes, *French Patent*, Application 1000186903, March 28, 2013.

[32] Yurkin M.A., Maltsev V.P., and Hoekstra A.G., Convergence of the discrete dipole approximation. I. Theoretical analysis, *Journal of the Optical Society of America A* **23**, 2578-2591, 2006.

[33] Yurkin M.A., Maltsev V.P., and Hoekstra A.G., Convergence of the discrete dipole approximation. II. An extrapolation technique to increase the accuracy, *Journal of the Optical Society of America A* **23**, 2592-2601, 2006.

[34] Christy R.W. and Johnson P.B., Optical constants of the noble metals, *Physical Review B* **6**, 4370-4379, 1972.

[35] Yurkin M.A., de Kanter D., and Hoekstra A.G., Accuracy of the discrete dipole approximation for simulation of optical properties of gold nanoparticles, *Journal of Nanophotonics* **4**, 041585, 2010.

CHAPTER 3

CONCLUSIONS

3.1 Summary

Through using the discrete dipole approximation with surface interaction (DDA-SI) as a forward model to predict scattering by objects on a surface, the Polarized-Surface-Wave-Scattering System (PSWSS) is primed to become a nanoscale characterization system to supplement current nanoscale imaging techniques. Far-field scattering predictions via DDA-SI have been validated against experimental results in the microwave regime with a very good agreement between the two. DDA-SI has also been improved for greater accuracy and expanded to include the amplitude scattering matrix elements and Mueller matrix elements; these programs are included in Appendices B-F. A sensitivity analysis of four Mueller matrix elements (M_{11}, M_{12}, M_{21}, M_{22}) has been performed of varying size, shape, material, and arrangement of gold and silver nanoparticles for application to the PSWSS.

Through the performed sensitivity analysis, it was found that the four Mueller matrix elements are sensitive to changes in shape and arrangement. This shows characterizing the state of agglomeration using the PSWSS is both possible and straightforward using the more easily measured Mueller matrix elements. Unfortunately, the four Mueller matrix elements proved insufficient to difference in material and sizes

smaller than one-half the wavelength of incident light. Characterization of more drastically different materials may still be possible using these four elements; however, gold and silver have very similar permittivities. For this case, and for particles smaller than one-half wavelength, analysis of other Mueller matrix elements that measure a change in circular polarization will be necessary; all of which is possible to model using the added DDA-SI programs, though a more arduous task to experimentally validate. In order to measure circular polarization, quarter wave plates must be added to the system. This will require more measurements as well as a loss in signal; hence the appeal of the four tested Mueller matrix elements.

Though more analysis is necessary for some functions of the PSWSS, these results show the impact the system can have in some applications, just as outlined in Chapter 1. If certain characteristics such as the material are not unknown, then even the four analyzed Mueller matrix elements may not be necessary to perform quality control measurements in a manufacturing or research environment. Furthermore, if only a certain size or shape distribution is being analyzed, then only a small range of scattering angle measurements may be necessary. All of this will lead to the possibility of even faster measurement times and higher sensitivity with the PSWSS. This shows that the combination of DDA-SI and the PSWSS is both robust and flexible enough to be optimized for many given applications.

3.2 Recommendations

While further sensitivity analysis is performed using DDA-SI, calibration samples are being prepared at Sandia National Laboratories and the University of Utah for

experimental results using the PSWSS. As part of the 2012 University Alliance MEMS Design Competition, an adjustable diffraction grating is being fabricated at Sandia National Laboratories [1]. Because a diffraction grating is an easily modeled scatterer, having a grating with adjustable spacing between 0 and 1 μm will function as both a validation and calibration tool for the PSWSS. Similarly, at the University of Utah, gold nanoscale cubes of varying size are being fabricated in arrays with varying spacing, similar to Figure 2.8. These are comparable to a 2-D diffraction grating and will also function as validation and calibration tools for the PSWSS.

Similarly, more extensive measurements will be taken using the microwave set-up at the Institut Fresnel in Marseille, France. In this work, only two geometries, a single sphere and a single cube, have been validated, both with a relatively low permittivity. Future experiments will include more elaborately shaped single objects, a wider range of sizes, as well as objects with much higher permittivities. Similar experiments will also take place using the PSWSS with nanoparticles as opposed to gratings or cubes. Using these experiments, a more thorough validation and expansion of DDA-SI will take place in order to begin building the scattering profile database. Once the scattering profile database of simulation results has been built using DDA-SI, the inversion will be tested using scattering profiles from known sources.

3.3 Conclusion

This thesis work has established DDA-SI as a robust forward model for the PSWSS to complement current nanoscale imaging technologies through unobtrusive, real-time characterization. It has been done through expansion of the program, validation

against experimental results, and a sensitivity analysis of four Mueller matrix elements. All results are submitted to be published in the *Journal of Quantitative Spectroscopy and Radiative Transfer*. Future research efforts will include more extensive experimental measurements using both the microwave set-up and the PSWSS in order to further validate DDA-SI, calibrate the PSWSS, and build the necessary scattering profile database. This will happen alongside further sensitivity analysis in preparation for characterization using the PSWSS.

3.4 References

[1] Hogan A.L., Frerck M., Passman J., Benardi M. P., Short M.R., Campbell J. and Harvey I. R., Audiovisual Enhancement through MEMS Micro Camcorder, Sandia University Alliance Design Competition Formal Paper and Invited Presentation, May 2012.

APPENDIX A

FUNDAMENTALS OF WAVE POLARIZATION, THE STOKES PARAMETERS, AND THE MUELLER MATRIX ELEMENTS

In order to better understand the PSWSS, necessary theoretical background is given below, including: wave polarization, the Stokes parameters, and the Mueller matrices.

A.1 Polarization

Before looking into more specific areas of electromagnetic wave scattering and the PSWSS, a better understanding of some electromagnetic wave theory must be developed, specifically wave polarization. Transverse electromagnetic waves such as light are fully characterized by four parameters: intensity, frequency or wavelength, direction of propagation, and state of polarization. Polarization is the orientation of the electric field oscillations, and is a necessary parameter to read in the scattering profile for the PSWSS. The first and most basic mode of polarization in these waves is linear polarization, or a *plane-polarized wave*. A wave propagating in the *z*-direction is considered, with two orthogonal electric fields, $\mathbf{E}_x$ and $\mathbf{E}_y$, and is given by the equations [1]:

$$\mathbf{E}_x(z,t) = \hat{\mathbf{i}} E_{0,x} \cos(kz - \omega t) \tag{A.1}$$

$$\mathbf{E}_y(z,t) = \hat{\mathbf{j}} E_{0,y} \cos(kz - \omega t + \varepsilon) \tag{A.2}$$

where E_0 is the fixed amplitude of the electric field in its given direction, k is the wavevector, ω is the angular frequency, t is time, and ε is the phase difference between the two waves, not to be confused with the same symbol used for permittivity. The resultant electric field **E**(z,t) is the sum of these two perpendicular waves:

$$\mathbf{E}(z,t) = \mathbf{E}_x(z,t) + \mathbf{E}_y(z,t) \tag{A.3}$$

It is apparent that when ε is equal to zero or a multiple of $\pm 2\pi$, the two perpendicular waves will be in-phase with one another, such that:

$$\mathbf{E}(z,t) = (\hat{\mathbf{i}}E_{0,x} + \hat{\mathbf{j}}E_{0,y})\cos(kz - \omega t) \tag{A.4}$$

where the first term, $(\hat{\mathbf{i}}E_{0,x} + \hat{\mathbf{j}}E_{0,y})$, is now the fixed amplitude of the wave. The plane in which this resultant vector oscillates is referred to as the plane of vibration. It is when this plane of vibration is constant that the wave is considered *linearly polarized*. Similar to the previous case, but if $\varepsilon = \pm\pi$, the two waves are said to be out-of-phase and take on the form:

$$\mathbf{E}(z,t) = (\hat{\mathbf{i}}E_{0,x} - \hat{\mathbf{j}}E_{0,y})\cos(kz - \omega t) \tag{A.5}$$

In this case, the wave is still linearly polarized, but now the plane of vibration has rotated by 180° from the in-phase case. The case of a linearly polarized wave is depicted in Figure A.1.

The second polarization mode of interest is circular polarization. This mode occurs when the component waves have equal amplitudes, such that $E_{0,x} = E_{0,y} = E_0$ and their phase difference $\varepsilon = -\pi/2 \pm 2\pi n$ (where n=0, ±1, ±2,…), in which case the resultant wave takes on the form [1]:

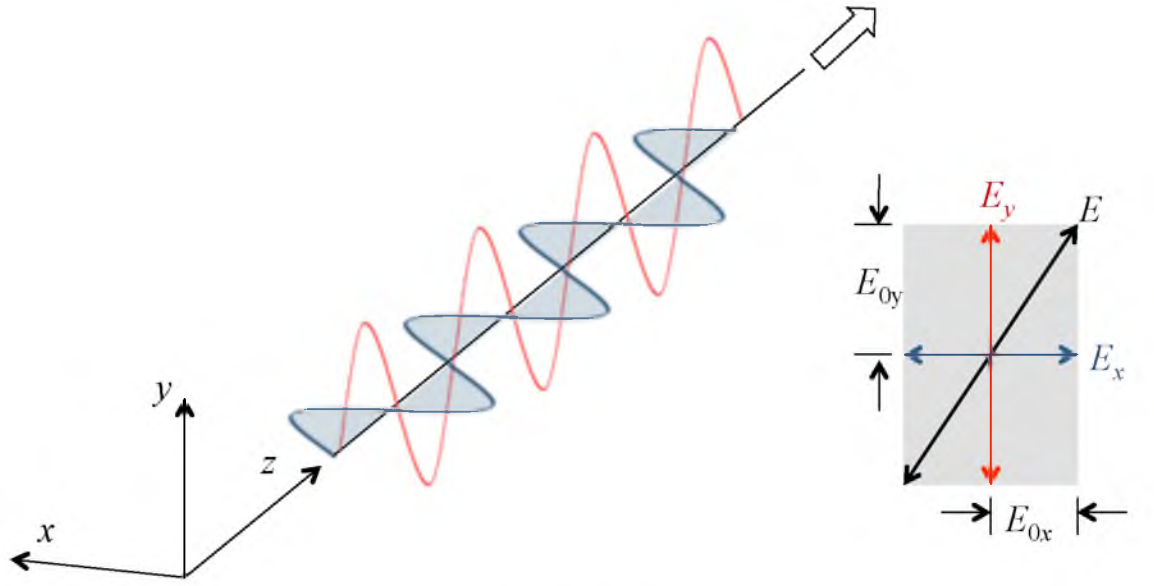

Figure A.1: Diagram of a linearly polarized wave [2]

$$\mathbf{E}(z,t) = E_0[\hat{\mathbf{i}}\cos(kz - \omega t) + \hat{\mathbf{j}}\sin(kz - \omega t)] \tag{A.6}$$

In this form, the fixed amplitude of the wave is constant and equal to E_0, but the second term, which governs the direction of oscillation, will now vary with time; this is the definition of a *circularly polarized wave*. For this particular wave, if an observer were to look along the z-axis towards the source of emission, this wave would rotate in the clockwise direction. This type of wave is referred to as *right-circularly polarized*, and is depicted in Figure A.2. Similarly, a *left-circularly polarized* wave occurs when the phase difference is $\varepsilon = \pi/2 \pm 2\pi n$ (where n=0, ±1, ±2,…), such that:

$$\mathbf{E}(z,t) = E_0[\hat{\mathbf{i}}\cos(kz - \omega t) - \hat{\mathbf{j}}\sin(kz - \omega t)] \tag{A.7}$$

where the same observer would see a wave rotating in the counter-clockwise direction.

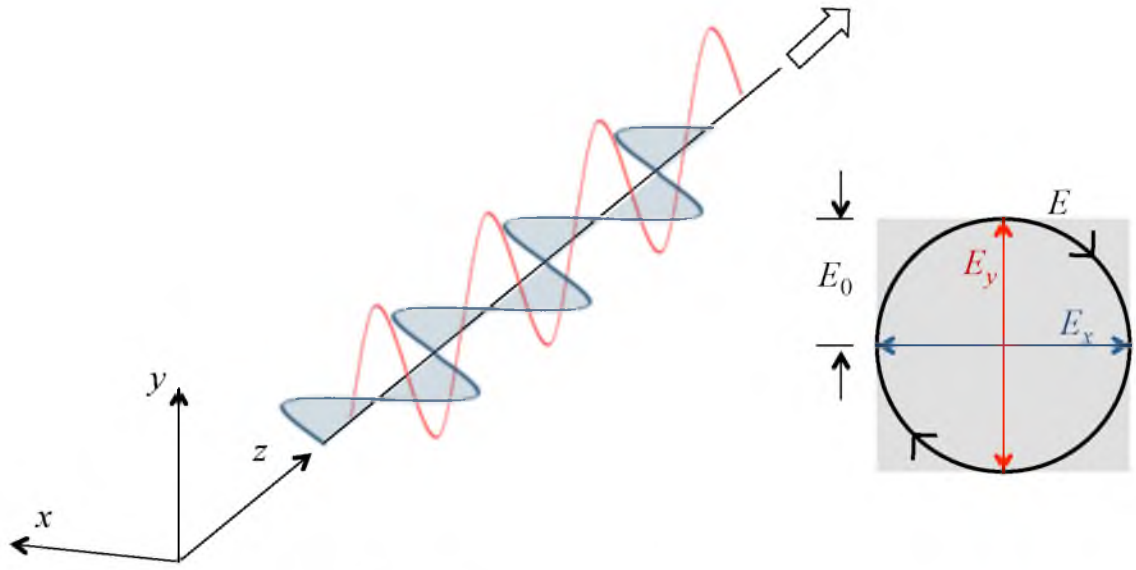

Figure A.2: Diagram of a right-circularly polarized wave [2]

It can also be shown that superimposing two circularly polarized waves of opposite rotation and equal amplitude can create a linearly polarized wave. If the equations for the last two circularly polarized waves are added, the resultant wave becomes:

$$\mathbf{E}(z,t) = 2E_0\hat{\mathbf{i}}\cos(kz-\omega t) \tag{A.8}$$

in which case the wave would be a linear wave with an amplitude of $2E_0$.

The last mode to be discussed is elliptical polarization, in which case both the direction and amplitude will vary with time. At first glance it may seem to be the most complicated mode of polarization, but it can also be seen that both circularly and linearly, polarized waves are only specific types of elliptically polarized waves. In the case of a circularly polarized wave, an observer viewing along the *z*-axis towards the source of

emission would see a circle drawn by the tip of the vector **E**; in the case of an elliptically polarized wave, an ellipse would be drawn. Using this idea, it can be shown that [1]:

$$\left(\frac{E_y}{E_{0,y}}\right)^2+\left(\frac{E_x}{E_{0,x}}\right)^2-2\left(\frac{E_x}{E_{0,x}}\right)\left(\frac{E_y}{E_{0,y}}\right)\cos(\varepsilon)=\sin^2(\varepsilon) \qquad \text{(A.9)}$$

where no assumption has been made in regards to ε, and the equation is that of an ellipse in the (E_x,E_y)-coordinate system forming an angle, α, with the horizontal E_x axis, as seen in Figure A.3.

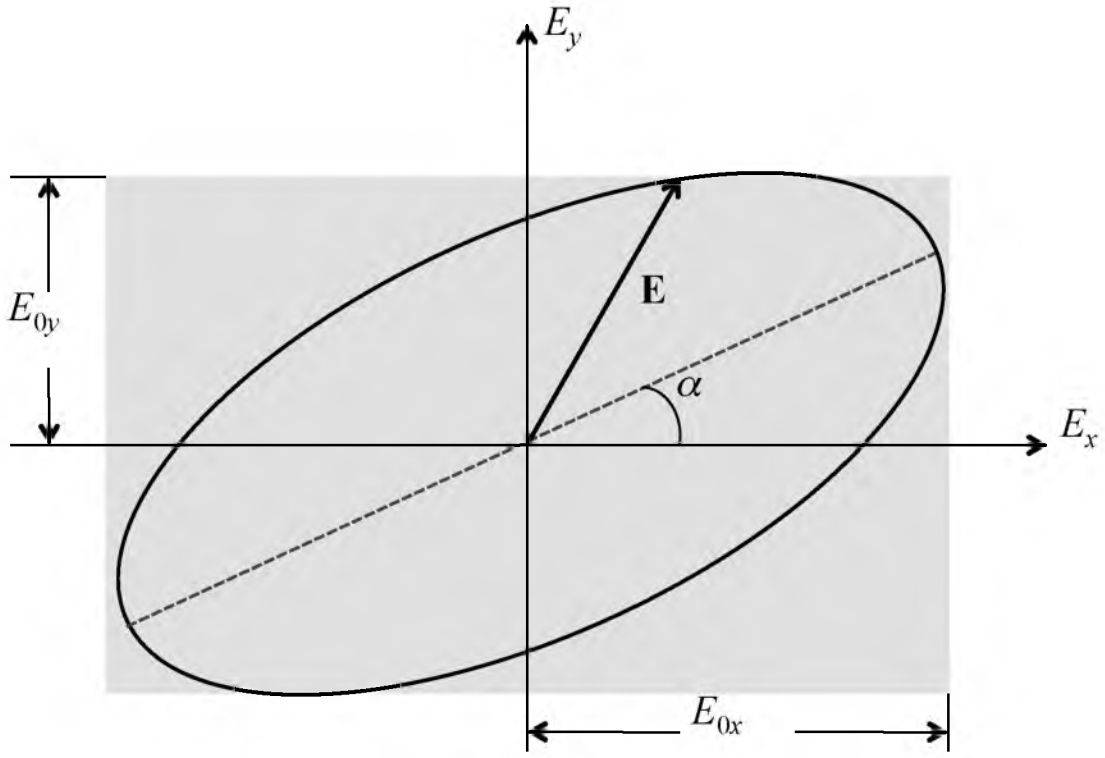

Figure A.3: Diagram of an elliptically polarized wave [2]

The following relationship can then be shown [2]:

$$\tan(2\alpha) = \frac{2E_{0,x}E_{0,y}\cos(\varepsilon)}{E_{0,x}^2 - E_{0,y}^2} \tag{A.10}$$

It can be seen if the assumptions of $E_{0,x} = E_{0,y} = E_0$ along with $\varepsilon = \pm\pi/2, \pm 3\pi/2, \pm 5\pi/2$, are applied, then an equation for a circle can be found. Also, if the assumption that ε is equal to an even multiple of π, then the equation of a line is found with the slope $\pm E_{0,x} / E_{0,y}$.

Given this knowledge of wave polarization, it is easier to understand that a polarizer is a device that imposes a specific polarization on a wave. Just as two circularly polarized waves can be combined to create a linear wave, waves can be manipulated and created through combinations of polarizers for varying results. A linear polarizer (LP) can impose linear polarization of a wave, as the name suggests. Similarly, a quarter wave plate (QWP) can enact a relative phase shift.

A.2 Stokes parameters

A detector can only measure intensity; however, polarization must also be measured in order to accomplish characterization. The Stokes parameters are a set of experimentally detectible parameters that can completely describe the polarization of a wave by using a few basic principles and combinations of polarizers and/or quarter wave plates. The parameters are broken up into four different sets, this set of parameters is also referred to as the Stokes vector.

Following similar methodology as [1-3], consider an incident beam of light that passes through four different filters separately, still propagating along the *z*-axis. The first of these filters has no polarization, such that the detector records the entire incident irradiance. This is the first of the four parameters, *I,* and is given by:

$$I = I_x + I_y = E_{0,x}E_{0,x}^* + E_{0,y}E_{0,y}^* \tag{A.11}$$

where I_x and I_y are the irradiance in their given direction. The irradiance, or intensity, is a real quantity, which can be measured by a detector, and is equal to the square of the magnitude of the fields, $E_{0,x}^2$ and $E_{0,y}^2$. In actuality, the irradiance accounts for both the real and imaginary parts of the wave. For this reason in the equations given, the complex conjugate, denoted by the superscript *, is introduced in order to account for the complex nature of the wave. The second filter examined is a linear polarizer and is used for two separate irradiance readings: one with the polarizer aligned parallel to the horizontal *x*-axis, the second with it aligned to the vertical *y*-axis. In each case, the polarizer is opaque to any transmission other than the part of the wave parallel to the orientation of the polarizer. The difference between these two experiments makes up the second of the Stokes parameters, *Q*, and is given by:

$$Q = I_x - I_y = E_{0,x}E_{0,x}^* - E_{0,y}E_{0,y}^* \tag{A.12}$$

Similarly, for the third parameter, two irradiance readings are taken. In this case, it is with a linear polarizer at +45° and -45° from horizontal. The third parameter, U, is given once again by the difference between the two readings:

$$U = I_{45^\circ} - I_{-45^\circ} = E_{0,x}E_{0,y}^{*} + E_{0,y}E_{0,x}^{*} \tag{A.13}$$

Lastly, there must be a test for the circular polarization of the wave. In order to accomplish this, two tests are once again performed: the first with a right-handed polarizer and the second with a left-handed polarizer. The difference between the two irradiances is taken to find the parameter, V, given from:

$$V = I_{RH} - I_{LH} = i(E_{0,y}^{*}E_{0,x} - E_{0,x}^{*}E_{0,y}) \tag{A.14}$$

These four variables make up the Stokes parameters, I, Q, U, and V, and in turn become the Stokes vector, **S**, of the form:

$$\mathrm{S} = \begin{pmatrix} I \\ Q \\ U \\ V \end{pmatrix} = \begin{pmatrix} E_{0,x}E_{0,x}^{*} + E_{0,y}E_{0,y}^{*} \\ E_{0,x}E_{0,x}^{*} - E_{0,y}E_{0,y}^{*} \\ E_{0,x}E_{0,y}^{*} - E_{0,y}E_{0,x}^{*} \\ i(E_{0,y}^{*}E_{0,x} - E_{0,x}^{*}E_{0,y}) \end{pmatrix} \tag{A.15}$$

The power behind this is that it gives the complete state of polarization of the wave and is experimentally measureable by measuring the intensity using combinations of LPs and QWPs. In the experimental sense, each parameter would actually be recorded as the

temporal or statistical average, in which case each term could be denoted with brackets⟨ ⟩.

A.3 Mueller matrices

Following the same methodology as outlined in [3], a Mueller matrix is a 4 by 4 matrix applied to the Stokes parameters of an incident beam in order to find the transmitted beam after interaction with an optical element (such as an LP, QWP, or any medium which changes the polarization state). In short, a Mueller matrix relates an incident electromagnetic field to a transmitted or scattered field. For example, consider the electric field of an incident field, ($E_{x,inc}$, $E_{y,inc}$), and the transmitted components given by, ($E_{x,trans}$, $E_{y,trans}$), after passing through a linear polarizer,

$$\begin{pmatrix} E_{x,trans} \\ E_{y,trans} \end{pmatrix} = \begin{pmatrix} \cos^2\xi & \sin\xi\cos\xi \\ \sin\xi\cos\xi & \sin^2\xi \end{pmatrix} \begin{pmatrix} E_{x,inc} \\ E_{y,inc} \end{pmatrix} \tag{A.16}$$

where ξ is the smallest angle between the transmission axis and the x-direction. A Mueller matrix is applied to a Stokes vector such that,

$$\begin{pmatrix} I \\ Q \\ U \\ V \end{pmatrix}_{trans} = \overline{\overline{\mathbf{M}}} \begin{pmatrix} I \\ Q \\ U \\ V \end{pmatrix}_{inc} \tag{A.17}$$

where an example of a Mueller matrix, $\overline{\overline{\mathbf{M}}}$, for a linear polarizer is of the form [3]:

$$\frac{1}{2}\begin{pmatrix} 1 & \cos 2\xi & \sin 2\xi & 0 \\ \cos 2\xi & \cos^2 2\xi & \cos 2\xi \sin 2\xi & 0 \\ \sin 2\xi & \sin 2\xi \cos 2\xi & \sin^2 2\xi & 0 \\ 0 & 0 & 0 & 0 \end{pmatrix} \tag{A.18}$$

Thus, if the transmission axis is along the *x*-direction and $\xi = 0$, the matrix becomes:

$$\frac{1}{2}\begin{pmatrix} 1 & 1 & 0 & 0 \\ 1 & 1 & 0 & 0 \\ 0 & 0 & 0 & 0 \\ 0 & 0 & 0 & 0 \end{pmatrix} \tag{A.19}$$

One important thing to note is that the matrix multiplication is not commutative. Just as in a physical set up of the optical components, each matrix must be applied in order. The power of these Mueller matrices, and their application to the PSWSS system, shows through in the fact that the same methodology can be applied in regards to the scattering of light by particles.

Similar to Eq. (A.16) where an incident wave becomes a transmitted wave through interaction with a polarizer, an incident wave can become a scattered wave through interaction with some media. The amplitude scattering matrix $\overline{\overline{\mathbf{S}}}$ represents this scattering interaction. In the following equation, the transmitted wave is now referred to as the scattered wave and the electric field is split up into the transverse magnetic (TM) and transverse electric (TE) parts of the wave. Similar to the transmitted case, the following equation can be found [2]:

$$\begin{pmatrix} E_{sca}^{TM} \\ E_{sca}^{TE} \end{pmatrix} = \frac{e^{ikr}}{ikr}\begin{pmatrix} S_2 & S_3 \\ S_4 & S_1 \end{pmatrix}\begin{pmatrix} E_{inc}^{TM} \\ E_{inc}^{TE} \end{pmatrix} = \frac{e^{ikr}}{ikr}(\overline{\overline{\mathbf{S}}})\begin{pmatrix} E_{inc}^{TM} \\ E_{inc}^{TE} \end{pmatrix} \tag{A.20}$$

where r is the distance from the scattering particle to the detector. It is the calculation of these four elements which had to be added to the DDA-SI program package, and from them, the Mueller matrix elements can be calculated [2-3].

As mentioned previously, experimental measurements of the Mueller matrix elements take place through measuring the incident and scattered Stokes vectors and using combinations of optical elements to only measure specific polarizations. This is shown by the equation:

$$\begin{pmatrix} I \\ Q \\ U \\ V \end{pmatrix}_{sca} = \frac{1}{k^2r^2}\begin{pmatrix} M_{11} & M_{12} & M_{13} & M_{14} \\ M_{21} & M_{22} & M_{23} & M_{24} \\ M_{31} & M_{32} & M_{33} & M_{34} \\ M_{41} & M_{42} & M_{43} & M_{44} \end{pmatrix}\begin{pmatrix} I \\ Q \\ U \\ V \end{pmatrix}_{inc} = \frac{1}{k^2r^2}\left(\overline{\overline{\mathrm{M}}}\right)\begin{pmatrix} I \\ Q \\ U \\ V \end{pmatrix}_{inc} \tag{A.21}$$

where each specific M_{ij} element of the $\overline{\overline{\mathbf{M}}}$ matrix can be found in [3]. It is also important to note that each matrix element is a function of the scattering angles (i.e., polar θ and azimuthal ϕ angles). While this scattering matrix is for a single particle, the scattering profile for a conglomeration of particles is the sum of the individual scattering matrices, just as in the case with optical elements. Given a measurement at various scattering angles of some or all of the Mueller matrix elements, the characteristics of the scattering media can be calculated.

A.4 References

[1] Hecht E., *Optics*, Pearson Education Inc., California, 2002.

[2] Francoeur M., Near-Field Radiative Transfer: Thermal Radiation, Thermophotovoltaic Power Generation and Optical Characterization, PhD Dissertation, University of Kentucky, 2010.

[3] Bohren C.F. and Huffman D.R., *Absorption and Scattering of Light by Small Particles*, Wiley, New York, 1983.

APPENDIX B

MATLAB PROGRAM – FAR-FIELD SCATTERING

```
%%% TEMPLATE FOR EVANESCENT ILLUMATION FOR FAR-FIELD SCATTERING %%%

clear all
clc

%%% INPUTS %%%

% INCIDENT WAVE INFORMATION
lambda=632.8;               % nm - Wavelength
gamma = 36*(pi/180);        % incident angle within substrate, measured
from normal

E1s = 1;                    % TE - Polarization
E1p = 0;                    % TM - Polarization
E0 = [E1s E1p];

% REFRACTIVE INDECIES
n1=1.7659;              % Sapphire Substrate as per Francoeur Thesis
n2=1;                   % Air
n3=n_Au(lambda);        % Gold Particle extrapolated from Johnson &
Christy

k = 2*pi;
k1=n1*k;
k2=n2*k;

% LOAD SPHERE GEOMETRY
D = 10;                          % nm - Diameter of Sphere
r = dlmread('sphere_552.txt'); % load sphere

[N,col] = size(r);                % N = no. of dipoles
a_eff = .5*D/lambda;              % effective radius, relative to
wavelength
d = (4/3*pi/N)^(1/3)*a_eff;       % lattice spacing based on Nd^3 = 4/3
pi r^3
r = d*r;                          % rescale sphere to wavelength units
r = [r(:,1) r(:,2) r(:,3)+a_eff]; % sit the sphere on the surface
m = n3*ones(N,1);
% m is N-length vector containing relative refractive indices(isotropic
version) for polarizability_LDR(d,m,kvec,E0)

% % OPTIONAL CUBE GEOMETRY
% sides = 450;                    % nm - length of sides of cube
% r = dlmread('cube_216.txt');
% [N,col] = size(r);
% m = n3*ones(N,1);
% nl = nthroot(N,3);
% r(:,3) = r(:,3) + nl/2;
% d = sides/nl/lambda;
% r = d*r;

% DETECTOR INFORMATION
theta = linspace(-pi/2,pi/2,360); % phase angle range
pts = length(theta);
phi_p = zeros(1,pts);
phi_s = pi/2*ones(1,pts);
det_r = 10000;               % nm detector distance
```

```
%%% CALCULATIONS %%%

% Generate evanescent wave
[kvec,E2s,E2p]=evanescent_E(E0(:,1),E0(:,2),gamma,n1,n2);
E2 = E2s+E2p;

% New Incident field via evanescent wave
Ei = E_inc(E2,kvec,r);

% DIPOLE INTERACTION
alph = polarizability_LDR(d,m,kvec,Ei);
AR = interaction_AR(k1,k2,r,alph); % formulate interaction matrix
P = qmr(AR, Ei,[],3000);           % solve dipole moments (various
iterative techniques could be used here)

% FRESNEL COEFFICIENT CALCULATIONS
f_angle=0;
[refl_TE,refl_TM] = Fresnel_coeff_n(n1,abs(f_angle));

% SCATTERED FIELD

% parallel to incident plane
rE_p = [det_r*ones(1,pts)' theta' phi_p'];
Esca_p =
E_sca_SI(k,r,P,rE_p(:,1),rE_p(:,2),rE_p(:,3),refl_TM,refl_TE,n1);
E_p = Esca_p;

% perpendicular to incident plane
rE_s = [det_r*ones(1,pts)' theta' phi_s'];
Esca_s =
E_sca_SI(k,r,P,rE_s(:,1),rE_s(:,2),rE_s(:,3),refl_TM,refl_TE,n1);
E_s = Esca_s;


%%% OUTPUTS %%%
th = theta'*180/pi;     % Theta for plots

% DIPOLE MODEL CHECK
figure(1)
clf
hold on
plot3(r(:,1)*lambda,r(:,2)*lambda,r(:,3)*lambda,'o','MarkerSize',3)
view(45,45)
axis equal on
hold off
xlabel('x (nm)')
ylabel('y (nm)')
zlabel('z (nm)')

% SCATTERING INTENSITY
I_p = k^2*(det_r.^2)'.*dot(E_p,E_p,2);
I_s = k^2*(det_r.^2)'.*dot(E_s,E_s,2);
I_tot=I_p+I_s;

figure(2)
clf
semilogy(th,I_s*10^21,'-',th,I_p*10^21,'--',th,I_tot*10^21,':')
```

```
ylabel('I_{sca} k^2 (det r)^2')
xlabel('Scattering Angle')
xlim([-85 85])
h=legend('I_s','I_p','I_{tot}');
set(h,'Location','NorthEast')
title(['N=' int2str(N)])

% AMPLITUDE PLOT FOR COMPARISON WITH MICROWAVE
Ax=E_s(:,1);
Ax=20*log10(abs(Ax));       % CONVERSTION TO dB SCALE

figure(3)
clf
plot(th,Ax)
ylabel('Ax')
xlabel('Scattering Angle')
h=legend('A_x','A_x -3^o','A_x +3^o','A_{x,exp}');
set(h,'Location','NorthEast')
xlim([-74 74])
```

APPENDIX C

MATLAB PROGRAM – MUELLER

MATRIX ELEMENTS

```
%%% TEMPLATE FOR EVANESCENT ILLUMATION FOR Mueller Matrix Elements %%%

clear all
clc

%%% INPUTS %%%

% INCIDENT WAVE INFORMATION
lambda= 632.8;          % nm - Wavelength
gamma = 36*(pi/180);    % incident angle within substrate, measured from
normal

% REFRACTIVE INDECIES
n1=1.7659;              % Sapphire Substrate as per Francoeur Thesis
n2=1;                   % Air
n3=n_Au(lambda);        % Gold Particle extrapolated from Johnson &
Christy

k = 2*pi;
k1= n1*k;
k2= n2*k;

% LOAD SPHERE GEOMETRY
D = 400;                            % nm - Diameter of Sphere

r = dlmread('sphere_3112.txt');     % load sphere
[N,col] = size(r);                  % N = no. of dipoles
a_eff = .5*D/lambda;                % effective radius, relative to
wavelength
d = (4/3*pi/N)^(1/3)*a_eff;         % lattice spacing based on Nd^3 = 4/3
pi r^3
r = d*r;                            % rescale sphere to wavelength units
r = [r(:,1) r(:,2) r(:,3)+a_eff]; % sit the sphere on the surface
m = n3*ones(N,1);
% m is N-length vector containing relative refractive indices(isotropic
version) for polarizability_LDR(d,m,kvec,E0)

% DETECTOR INFORMATION
theta = linspace(-pi/2,pi/2,360); % phase angle range
th = theta'*180/pi;                 %Theta for plots
pts = length(theta);
det_r = 10000;                      % nm detector distance

% % OPTIONAL CUBE GEOMETRY
% sides = 450;                      % nm - length of sides of cube
% r = dlmread('cube_216.txt');
% [N,col] = size(r);
% m = n3*ones(N,1);
% nl = nthroot(N,3);
% r(:,3) = r(:,3) + nl/2;
% d = sides/nl/lambda;
% r = d*r;

% This is counter to run through twice for TE & TM in order to get all
4 S
% matrix elements for Mueller Matrix calculation

for count=1:2;
```

```
% For TE Polarization
if count==2;
    phi_p = zeros(1,pts);
    phi_s = pi/2*ones(1,pts);
    E1s = 1;                        % TE - Polarization
    E1p = 0;                        % TM - Polarization
    E0 = [E1s E1p];
% For TM Polarization
else
    phi_p = pi/2*ones(1,pts);
    phi_s = zeros(1,pts);
    E1s = 0;                        % TE - Polarization
    E1p = 1;                        % TM - Polarization
    E0 = [E1s E1p];
end

%%% CALCULATIONS %%%
[kvec,E2s,E2p]=evanescent_E(E0(:,1),E0(:,2),gamma,n1,n2); % Generate
evanescent wave
E2 = E2s+E2p;
Ei = E_inc(E2,kvec,r);            % New Incident field via evanescent
wave

% DIPOLE INTERACTION
alph = polarizability_LDR(d,m,kvec,Ei);
AR = interaction_AR(k1,k2,r,alph);                % formulate
interaction matrix
P = qmr(AR, Ei,[],8000);                          % solve dipole
moments (various iterative techniques could be used here)
f_angle=0;
[refl_TE,refl_TM] = Fresnel_coeff_n(n1,abs(f_angle));

rE_p = [det_r*ones(1,pts)' theta' phi_p'];
rE_s = [det_r*ones(1,pts)' theta' phi_s'];

Cext=C_ext(k,E0,Ei,P);
Cabs=C_abs(k,E0,Ei,P,alph);
Csca=Cext-Cabs;
Qext=Cext/(pi*a_eff^2);
Qabs=Cabs/(pi*a_eff^2);
Qsca=Csca/(pi*a_eff^2);


if count==2; %TE
    [S3] =
S_amp_scat_TE(k,r,P,rE_p(:,1),rE_p(:,2),rE_p(:,3),refl_TM,refl_TE,n1);
%TM/p Scattered Field
    [S1] =
S_amp_scat_TE(k,r,P,rE_s(:,1),rE_s(:,2),rE_s(:,3),refl_TM,refl_TE,n1);
%TE/s Scattered Field

    Cext_TE=Cext;
    Cabs_TE=Cabs;
    Csca_TE=Csca;
    Qext_TE=Qext;
    Qabs_TE=Qabs;
    Qsca_TE=Qsca;
```

```
else          %TM
    [S2] =
S_amp_scat_TM(k,r,P,rE_p(:,1),rE_p(:,2),rE_p(:,3),refl_TM,refl_TE,n1);
%TM/p Scattered Field
    [S4] =
S_amp_scat_TM(k,r,P,rE_s(:,1),rE_s(:,2),rE_s(:,3),refl_TM,refl_TE,n1);
%TE/s Scattered Field

    Cext_TM=Cext;
    Cabs_TM=Cabs;
    Csca_TM=Csca;
    Qext_TM=Qext;
    Qabs_TM=Qabs;
    Qsca_TM=Qsca;
end
end

% Calculate the Mueller Matrix Elements
[M] = muellermatrix(S1,S2,S3,S4,theta);

% PLOT OF 4 MUELLER MATRIX ELEMENTS
figure (1)
subplot(2,2,1);
semilogy(th,squeeze(M(1,1,:)));
h=legend('M11');
subplot(2,2,2);
plot(th,squeeze(M(1,2,:)));
h=legend('M12');
subplot(2,2,3);
plot(th,squeeze(M(2,1,:)));
h=legend('M21');
subplot(2,2,4);
plot(th,squeeze(M(2,2,:)));
h=legend('M22');

% Save data files for all Mueller Elements and Save figure
M_file = ['PSWSS_Gold_' num2str(D) 'nm_M_N' num2str(N)];
save(M_file,'M');
M_fig = ['PSWSS_Gold_' num2str(D) 'nm_M_N' num2str(N)];
hgsave(M_fig);
```

APPENDIX D

MATLAB SUBROUTINE – STOKES

AMPLITUDE SCATTERING

ELEMENTS

```
% Amplitude Scattering Matrix Elements for TE-Incidence
% Modification of E_sca_SI provided by Loke and Draine & Flatau

function [S1,S3] =
S_amp_scat_TE(k,r,P,det_r,theta,phi,refl_TM,refl_TE,n1)
% k: wave vector
% r: dipole coordinates (N x 3 matrix)
% P: polarizations (vector of length 3N; Px1,Py1,Pz1 ... PxN,PyN,PzN)
% Note: coordinates are relative to origin

[N,cols] = size(r);
[rows,cols] = size(theta);
if cols > rows
  theta = reshape(theta,cols,rows);
end
[rows,cols] = size(phi);
if cols > rows
  phi = reshape(phi,cols,rows);
end
[rows,cols] = size(det_r);
if cols > rows
  det_r = reshape(det_r,cols,rows);
end

r_sp = [det_r theta phi];
[pts,cols] = size(r_sp);
r_unit = ones(pts,1);
er_sp = [r_unit theta phi];
e1_sp = [r_unit theta+sign(theta)*pi/2 phi];

r_E = rtp2xyz(er_sp);
r_E1 = rtp2xyz(e1_sp);
er = zeros(pts,3);
e1 = zeros(pts,3);
e2 = zeros(pts,3);

for j = 1:pts
  er(j,:) = r_E(j,:)/norm(r_E(j,:));
  e1(j,:) = r_E1(j,:)/norm(r_E1(j,:));
  e2(j,:) = cross(er(j,:),e1(j,:));
end

S1 = zeros(pts,3);
S3 = zeros(pts,3);

for pt = 1:pts
  erp = er(pt,:); %e_r
  e1p = e1(pt,:); %e_theta
  e2p = e2(pt,:); %e_phi
  k_sca = k*erp;
  k_Isca = [k_sca(1) k_sca(2) -k_sca(3)];

ref_angle=abs((-pi/2)+(pt-1)*pi/length(theta));
[refl_TE,refl_TM] = Fresnel_coeff_n(n1,abs(ref_angle));

rp = det_r(pt);
  for j = 1:N
    Pj = P(3*(j-1)+1:3*(j-1)+3);
```

```
    rj = r(j,:);
    rIj = [rj(1) rj(2) -rj(3)];

%%% Amplitude Scattering Elements S1 & S3 (For Pj(2) - TE Incident)
    S1(pt,:) = S1(pt,:) + (exp(-1i*dot(k_sca,rj))+refl_TE*exp(-
1i*dot(k_sca,rIj)))*dot(Pj,e2p);
    S3(pt,:) = S3(pt,:) + (exp(-1i*dot(k_sca,rj))+refl_TM*exp(-
1i*dot(k_sca,rIj)))*dot(Pj,e1p);

  end
  c=(-1i*k^3)/(4*pi*8.8541878*10^-12);
  S1(pt,:) = S1(pt,:).*c;
  S3(pt,:) = S3(pt,:).*c;
end
  S1 = S1(:,1);
  S3 = S3(:,1);

% Amplitude Scattering Matrix Elements for TM-Incidence
% Modification of E_sca_SI provided by Loke and Draine & Flatau

function [S2,S4] =
S_amp_scat_TM(k,r,P,det_r,theta,phi,refl_TM,refl_TE,n1)
% k: wave vector
% r: dipole coordinates (N x 3 matrix)
% P: polarizations (vector of length 3N; Px1,Py1,Pz1 ... PxN,PyN,PzN)
% Note: coordinates are relative to origin

[N,cols] = size(r);

[rows,cols] = size(theta);
if cols > rows
  theta = reshape(theta,cols,rows);
end
[rows,cols] = size(phi);
if cols > rows
  phi = reshape(phi,cols,rows);
end
[rows,cols] = size(det_r);
if cols > rows
  det_r = reshape(det_r,cols,rows);
end

r_sp = [det_r theta phi];
[pts,cols] = size(r_sp);
r_unit = ones(pts,1);
er_sp = [r_unit theta phi];
e1_sp = [r_unit theta+sign(theta)*pi/2 phi];
r_E = rtp2xyz(er_sp);
r_E1 = rtp2xyz(e1_sp);
er = zeros(pts,3);
e1 = zeros(pts,3);
e2 = zeros(pts,3);

for j = 1:pts
  er(j,:) = r_E(j,:)/norm(r_E(j,:));
  e1(j,:) = r_E1(j,:)/norm(r_E1(j,:));
  e2(j,:) = cross(er(j,:),e1(j,:));
end
```

```
S2 = zeros(pts,3);
S4 = zeros(pts,3);

for pt = 1:pts
  erp = er(pt,:); %e_r
  e1p = e1(pt,:); %e_theta
  e2p = e2(pt,:); %e_phi
  k_sca = k*erp;
  k_Isca = [k_sca(1) k_sca(2) -k_sca(3)];

ref_angle=abs((-pi/2)+(pt-1)*pi/length(theta));
[refl_TE,refl_TM] = Fresnel_coeff_n(n1,abs(ref_angle));

rp = det_r(pt);
  for j = 1:N
    Pj = P(3*(j-1)+1:3*(j-1)+3);
    rj = r(j,:);
    rIj = [rj(1) rj(2) -rj(3)];

%%% Solve for Amplitude Scattering Matrix elements S2 & S4 (TM
incident)
    S2(pt,:) = S2(pt,:) + (exp(-1i*dot(k_sca,rj))+refl_TM*exp(-
1i*dot(k_sca,rIj)))*dot(Pj,e1p);
    S4(pt,:) = S4(pt,:) + (exp(-1i*dot(k_sca,rj))+refl_TE*exp(-
1i*dot(k_sca,rIj)))*dot(Pj,e2p);

  end
  c=(-1i*k^3)/(4*pi*8.8541878*10^-12);
  S2(pt,:) = S2(pt,:).*c;
  S4(pt,:) = S4(pt,:).*c;
  end

  S2 = S2(:,1);
  S4 = S4(:,1);
```

APPENDIX E

MATLAB SUBROUTINE – MUELLER

MATRIX ELEMENTS

```
% Mueller Matrix Element Calculations

function
[M11,M12,M13,M14,M21,M22,M23,M24,M31,M32,M33,M34,M41,M42,M43,M44] =
mueller(S1,S2,S3,S4)

M11=1/2*(abs(S1).^2+abs(S2).^2+abs(S3).^2+abs(S4).^2);
M12=(1/2*(abs(S2).^2-abs(S1).^2+abs(S4).^2-abs(S3).^2))./M11;
M13=(real(S2.*conj(S3)+S1.*conj(S4)))./M11;
M14=(imag(S2.*conj(S3)-S1.*conj(S4)))./M11;
M21=(1/2*(abs(S2).^2-abs(S1).^2-abs(S4).^2+abs(S3).^2))./M11;
M22=(1/2*(abs(S2).^2+abs(S1).^2-abs(S4).^2-abs(S3).^2))./M11;
M23=(real(S2.*conj(S3)-S1.*conj(S4)))./M11;
M24=(imag(S2.*conj(S3)+S1.*conj(S4)))./M11;
M31=(real(S2.*conj(S4)+S1.*conj(S3)))./M11;
M32=(real(S2.*conj(S4)-S1.*conj(S3)))./M11;
M33=(real(S1.*conj(S2)+S3.*conj(S4)))./M11;
M34=(imag(S2.*conj(S1)+S4.*conj(S3)))./M11;
M41=(imag(conj(S2).*S4+conj(S3).*S1))./M11;
M42=(imag(conj(S2).*S4-conj(S3).*S1))./M11;
M43=(imag(S1.*conj(S2)-S3.*conj(S4)))./M11;
M44=(real(S1.*conj(S2)-S3.*conj(S4)))./M11;
```

APPENDIX F

MATLAB PROGRAM – MODIFICATION OF '*E_sca_SI.m*'

PROGRAM FOR FRESNEL REFLECTION

COEFFICIENTS

The lines of code below were added to the '*E_sca_SI.m*' subroutine in order to calculate the Fresnel reflection coefficients at the angle of each dipole. Originally the Fresnel reflection coefficients were not calculated within the program and were a singular input to the sub-routine. This addition is within the '*E_sca_SI.m*' immediately following the calculation of the wave vector and image wave vector, k_{sca} and $k_{I,sca}$.

```
%%% This is the modification made to account for a Fresnel coef.
calculation at each angle of dipole
  ref_angle=abs((-pi/2)+(pt-1)*pi/length(theta));
  [refl_TE,refl_TM] = Fresnel_coeff_n(n1,abs(ref_angle));
```